Tesis Doctoral

STRETCHING LIQUID FLOWS: JETS, DROPS AND LIQUID BRIDGES

Experiments and one-dimensional modelling of linear and non-linear phenomena in laminar capillary flows

Autor
Mariano Rubio Rubio

Director
Alejandro Sevilla Santiago

DEPARTAMENTO DE INGENIERÍA TÉRMICA Y DE FLUIDOS

Leganés, febrero 2016

Tesis doctoral

STRETCHING LIQUID FLOWS: JETS, DROPS AND LIQUID BRIDGES

Autor: Mariano Rubio Rubio

Director de Tesis: Alejandro Sevilla Santiago

Firma del Tribunal Calificador:

Firma

Presidente
D. Ignacio González Loscertales
Secretario
Dña. Rocío Bolaños Jiménez
Vocal
D. Mark Blyth

Calificación:

Leganés, 5 de febrero de 2016

DEPARTAMENTO DE INGENIERÍA TÉRMICA Y DE FLUIDOS
Escuela Politécnica Superior

PhD Thesis

STRETCHING LIQUID FLOWS: JETS, DROPS AND LIQUID BRIDGES

Experiments and one-dimensional modelling of linear and non-linear phenomena in laminar capillary flows

Interuniversity Ph.D. Program in Fluid Mechanics

Author
Mariano Rubio Rubio

PhD Advisor
Alejandro Sevilla Santiago

Leganés, February 2016

Whether you can observe a thing or not
depends on the theory which you use.
It is the theory which decides what can be observed.

No amount of experimentation can ever prove me right;
a single experiment can prove me wrong.

Albert Einstein

Agradecimientos

Uno se precia de guardar consigo las lecciones más importantes que recibe. Entre ellas, está la de ser agradecido con la gente que lo merece. Al final de este viaje, y ante la incertidumbre del comienzo de uno nuevo, no quisiera dejar pasar la ocasión de dar las gracias a quienes, de una forma u otra, me han acompañado.

A Alejandro, mi director de Tesis, por darme la oportunidad de realizar este trabajo, y por su ayuda para que haya salido adelante. Por haberme enseñado parte de lo que sabe. Por la paciencia que ha demostrado al ser alguien como yo quien tiene que aprender. Por la ilusión con la que ha vivido cada uno de mis pequeños pasos.

Gracias, también, a Antonio Soria, que siempre está cuando hace falta, ya sea para una buena idea, un consejo o un rato de charla. Siempre estaré agradecido a Jorge por todo lo que hizo y sigue haciendo por mí desde que llegué a la UC3M. A ambos, por siempre tener palabras de ánimo, aparte de creer en mí.

During my PhD I have been abroad on two short reseach stays. I would like to thank Prof. Christian Clasen for granting me the possibility to learn almost like a member of the SMaRT group in KU Leuven. Particularly, thanks to Wouter for being so kind and helping me during my time in Leuven.

I also had the opportunity of visiting the IRPHE in Marseille, thanks to Prof. Emmanuel Villermaux. I would like to acknowledge the chance of collaborating and learning with him, summarized in his sentence 'I have always time for science'. I am also very grateful to Laurent Duchemin for both his help and kindness while I was in Marseille.

Durante estos años, han sido muchos los momentos compartidos con los compañeros del Departamento, así que la lista de agradecimientos es larga. Gracias a los profesores del grupo de Mecánica de Fluidos por su ayuda y disposición cuando ha sido necesario. En particular, a Mario, que siempre tiene un rato para contestar mis preguntas; y a Imma, aparte de por su paciencia conmigo administrando Caracol, por todo lo que me ha ayudado, y sigue, en la

docencia. A los profesores permanentes del grupo ISE, especialmente a Néstor, por preocuparse por mí como lo hace, aunque sea en el fondo. También Merche, Ulpiano y Domingo. No deben faltar en la lista Paula y Juan, porque pasar tanto tiempo conmigo no es, soy plenamente consciente de ello, nada fácil. Gracias al resto de compañeros 'jóvenes' del Departamento, por hacer agradable y, casi siempre, divertido ir a trabajar cada día. Y porque algunos son, desde hace tiempo, más amigos que compañeros. Particularmente Luismi, porque no se puede ser más buena gente que él, y lo demuestra cada poco; y Edu, porque compartir ratos de relax no está reñido con echar una mano cuando hace falta.

A mi familia y amigos les debo demasiado tiempo, así que no queda sino agradecerles su comprensión y, también, que me hayan apoyado los unos, y decidido seguir estando ahí los otros.

A mis padres, Cheo y Yoli, por tener confianza ciega en mí y en lo que hago, sin importarles qué sea.

Abstract

The present Ph.D. Thesis deals with several linear and non-linear phenomena present in extensional laminar capillary flows, such as jets, drops and liquid bridges.

When dispensing liquid from a vertical injector in the presence of gravity, drops grow at the outlet until the surface tension forces can no longer balance their weight and the pinch-off occurs. This dripping regime does not exist above a critical flow rate, at which an abrupt transition to jetting takes place. The parameters governing this transition are the liquid properties, the injector radius and the liquid flow rate.

In this Thesis, experiments and global linear stability analysis are employed to obtain the critical flow rate below which a liquid jet stretched by gravity is no longer steady. The theoretical description, based on the one-dimensional mass and momentum equations retaining the exact expression of the interfacial curvature, accurately predicts the onset of jet self-excited oscillations experimentally observed for wide ranges of liquid viscosity and nozzle diameter. The analysis reveals the essential stabilizing role played by the axial curvature of the jet, being this effect especially relevant for injectors with a large enough diameter. The results obtained allow to conclude that, surprisingly, the size of the steady threads produced at a given distance from the exit can be reduced by increasing the nozzle diameter.

Detailed descriptions of the rich dynamics of both the dripping regime and the transition to jetting are available in the literature, but only for small injector sizes. Therefore, new experiments on the dripping dynamics and jetting transition for a wide range of both liquid viscosities and injector diameters are presented in this work. The results reveal the existence of new regimes of dripping, which had not been observed before. In addition, the hysteresis present in the dripping-jetting transition, previously measured only for the case of water, is quantified for a liquid of higher viscosity for the first time.

The detailed characterization of the necking and pinching dynamics of drops is often studied through the thinning process of an axially stretched liquid

bridge. In this context, recent works on the capillary break-up of particulate suspensions show how the presence of particles modifies the expected thinning behaviour of a liquid bridge. Nevertheless, in this kind of experiments the final stage close to the pinch-off is not well understood yet. In this dissertation, the different thinning velocities present near the pinch-off of particle suspensions in a Newtonian matrix are modelled. To that end, the liquid trapped between two end particles of finite diameter is considered as a stretching Newtonian liquid bridge with a non-uniform prescribed motion of the boundaries. The model, based on the one-dimensional mass and momentum conservation equations, shows quantitative agreement with the experimental thinning and final pinching behaviour of suspending medium between individually monitored particles in the suspension. Comparison of the model predictions with experiments of suspensions with different particle sizes, volume fractions and matrix viscosities confirms that the developed model constitutes an excellent tool to improve the understanding of the detailed pinch-off mechanism of particle suspensions and, importantly, allows to conclude that the description of the final stages does not require non-Newtonian modelling.

Resumen

En la presente Tesis Doctoral se estudian algunos fenómenos lineales y no lineales novedosos presentes en flujos de líquido en aire sometidos a estiramiento axial, como es el caso de chorros, gotas y puentes líquidos.

Cuando se suministra un caudal constante de líquido a través de un inyector vertical en presencia de la gravedad, se forman en la salida gotas que crecen hasta que las fuerzas de tensión superficial no pueden contener el peso del fluido, produciéndose el desprendimiento de la gota. Este régimen de goteo deja de existir por encima de un caudal crítico, en el cual se produce una abrupta transición que da lugar a un chorro. Los parámetros que gobiernan esta transición son las propiedades del líquido, el radio del inyector y el caudal de líquido inyectado.

En esta Tesis se emplea un análisis de estabilidad global, así como experimentos, para obtener el caudal crítico por debajo del cual un chorro de líquido newtoniano estirado por gravedad deja de ser estacionario. La descripción teórica, basada en las ecuaciones unidimensionales de continuidad y cantidad de movimiento en las que se retiene la expresión exacta de la curvatura, predice de manera precisa la aparición de oscilaciones autoexcitadas observadas en los experimentos, para rangos amplios de viscosidades del líquido y diámetros de inyección. El análisis revela el esencial papel estabilizante de la curvatura axial, siendo este efecto especialmente relevante en inyectores con un diámetro suficientemente grande. Los resultados obtenidos permiten concluir que, sorprendentemente, el diámetro del filamento líquido estacionario a una distancia dada de la salida puede reducirse incrementando el diámetro de la tobera de inyección.

En la literatura pueden encontrarse descripciones detalladas de la dinámica tanto del régimen de goteo como de la transición al chorro, pero únicamente para tamaños de inyector suficientemente pequeños. Por ello, en este trabajo se presentan nuevos experimentos sobre la dinámica del goteo y la transición al régimen de chorro, para un amplio rango de viscosidades del líquido de trabajo y radios de inyector. Los resultados revelan la existencia de regímenes de goteo

que no habían sido observados con anterioridad. Además, la histéresis presente en las transiciones goteo-chorro, que había sido determinada sólo para el caso del agua, se cuantifica para el caso de un líquido de mayor viscosidad.

La caracterización detallada de la dinámica de formación de un cuello en la superficie libre del líquido y su posterior rotura por estiramiento es a menudo estudiada a través del proceso de estrechamiento radial de un puente líquido estirado axialmente. En este contexto, trabajos recientes en la rotura capilar de suspensiones coloidales muestran cómo la presencia de partículas modifica el comportamiento del puente líquido. Sin embargo, la etapa final cercana a la rotura no está aún completamente entendida. En este estudio se modelan las diferentes etapas de estrechamiento que existen cerca de la rotura por estiramiento de suspensiones de partículas en una matriz newtoniana. Para ello, el líquido atrapado entre dos partículas de tamaño finito es considerado como un puente líquido newtoniano, que se estira axialmente obedeciendo a un movimiento impuesto y no uniforme de sus extremos. El modelo, basado en las ecuaciones unidimensionales de conservación, muestra un excelente acuerdo cuantitativo si se usan como condiciones de contorno los resultados experimentales de dos partículas individuales monitorizadas en la suspensión. La comparación de las predicciones del modelo con experimentos de suspensiones con distintos tamaños de partícula, concentraciones y viscosidades de la matriz confirma que el modelo desarrollado constituye una excelente herramienta para mejorar el conocimiento de los mecanismos detallados de rotura de suspensiones de partículas, y permite concluir que la descripción de las etapas finales no requiere un modelado no newtoniano de la suspensión.

Contents

CHAPTER
ONE

Introduction: stretched capillary flows

Surface-tension-driven flows and, in particular, their tendency to fissure unbiddenly into drops have attracted the attention of scientists for more than three centuries, and the earliest systematic experiments can be found in the beginning of the 19th century. Fragmentation of jets and liquid sheets, formation of spume or sea spray by the wind blowing over the air-liquid interface, bursting phenomena upon an impact, and raindrops are different examples of transitions between a compact liquid volume and a dispersion of stable drops. As an example, Figure 1.1 shows two photographs by Harold Edgerton that clearly illustrate the intricate dynamics involved in the motion of free surfaces, and reveal the formation of drops.

In the liquid flows mentioned above, encountered everywhere in nature, industry and basic science, instabilities give rise to ligaments that constitute the sinews of atomization. Rayleigh, Plateau, and Maxwell developed the linear stability theory that explains the onset of break-up, but the non-linear behaviour near the pinch-off of drops has only recently received attention due to its relevance for a number of industrial applications, going from printing to mixing, for instance.

The cohesive nature of liquids originates the surface tension effects that, paradoxically, induce the break-up of jets, drops and liquid bridges. These flows thus serve as a *chef d'oeuvre* for free-surface dynamics, hydrodynamic instability and singularity formation leading to drop break-up, being an ideal inquest for liquid properties, such as surface tension, viscosity or non-Newtonian rheology, apart from their practical usefulness.

1.1 Liquid jets

The controlled generation of micron or sub-micron sized threads, films, drops and bubbles is central to many applications in medicine, pharmaceutics, chem-

Figure 1.1: Two photographs taken by Harold Edgerton. On the left, "Water from a faucet", the first one that Edgerton ever made that was not of a motor, in 1932. On the right, a lawn sprinkler creating an impressive figure eight as the water twists and disrupts into drops, taken in 1939. From Edgerton Digital Collection. © 2010 MIT.

ical engineering and materials science (see e.g. Barrero & Loscertales, 2007; Eggers & Villermaux, 2008; Rodríguez-Rodríguez *et al.*, 2015, and references therein).

The many different types of devices which, up to now, have been designed for the production of such tiny structures, usually rely on generating highly stretched thin fluid threads with diameters substantially smaller than that of the injector. This is done with the purpose of avoiding the difficulties associated with the fabrication and use of micron-sized solid geometries.

For instance, in fiber spinning applications (Pearson & Matovich, 1969; Denn, 1980; Stokes *et al.*, 2014), the narrowing effect on the jet is promoted through its coupling with a rotating spinerett. In electrospinning devices (Doshi & Reneker, 1995; Loscertales *et al.*, 2002; Marín *et al.*, 2007), the desired strong stretching of the liquid column is caused by the tangential electrical stresses acting on the jet surface. Another example is the use of a faster outer coflow and its associated favourable pressure gradient, which has proven to be an efficient method for the generation of highly stretched microjets which, thanks to the action of capillary instabilities, cause the disintegration of the innermost fluid into microdrops or microbubbles (Gañán-Calvo, 1998; Marín *et al.*, 2009; Gordillo *et al.*, 2014). As an example, Figure 1.2 shows experimental images of highly stretched compound jets in an electrospinning setup devoted to achieve micro- and nano-encapsulations, while in Figure 1.3 different regimes of a viscous coflow are depicted.

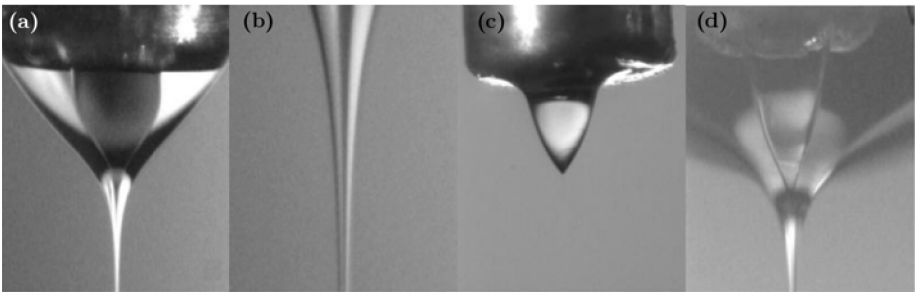

Figure 1.2: Structured Taylor cone (a) and downstream detail of two coaxial jets (b) emitted from the vertexes of the two menisci in a electrospinning device. A Taylor cone of water coated by a thin shell of olive oil (c), and by a thick shell of olive oil (d). Adapted from Loscertales *et al.* (2002).

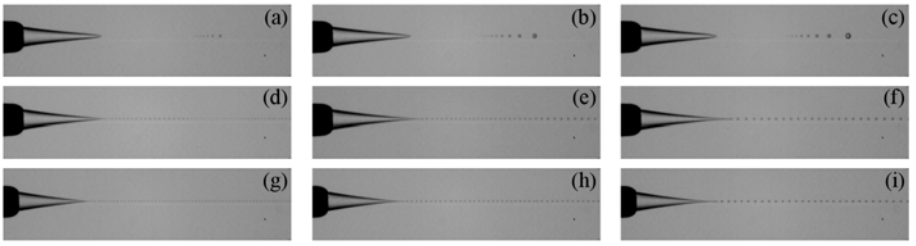

Figure 1.3: Images showing the generation of micro-emulsions in a coflow configuration, when varying the flow rate and viscosity ratios. From Gordillo *et al.* (2014).

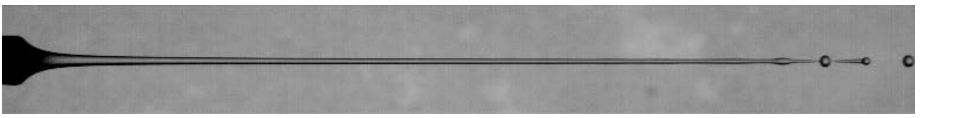

Figure 1.4: Globally stable jet of PDMS silicone oil with kinematic viscosity $\nu = 20$ cSt, injected vertically downwards through a tube of outer radius $R = 2.5$ mm at a constant flow rate $Q = 12.1$ ml/min.

Alternatively, Figure 1.4 shows that gravity can also induce the desired stretching effect on the jet formed when a liquid is injected though a vertically orientated tube. Indeed, the case depicted in Figure 1.4 constitutes an example of the so called 'jetting regime' in which a long filament develops when the imposed flow rate is above a certain threshold that depends on the liquid properties, the gravitational acceleration, and the radius of the injector.

Under these jetting conditions gravity accelerates the liquid downwards and, as a consequence of the conservation of the liquid flow rate, the jet narrows downstream and disrupts into drops with diameters significantly smaller than that of the injection tube. A recent work on the effect of gravity on the shape of viscous capillary jets is due to Montanero *et al.* (2011), where a comparison between numerical simulations and different models is performed. If the gravitational effects are negligible, as occurs for small injection diameters, or in microgravity environments, the diameters of the drops formed downstream in this jetting regime are comparable to the injector size (Suñol & González-Cinca, 2015).

The capillary break-up at some point downstream along the jet occurs naturally, due to the growth of small disturbances that are present in any environment, leading to break-up lengths and droplet sizes with a certain standard deviation because of the unavoidable noise in the facility. In the particular case of strongly axially stretched jets, of interest for this dissertation, a recent work that also uses one-dimensional modelling, as will be done in this Thesis, is due to Consoli-Lizzi *et al.* (2014). However, the possibility of generating monodisperse drops arises if the break-up is controlled by forcing the flow using e.g. electromagnetic or piezoelectric actuators. For instance, García *et al.* (2014) have recently derived a model to predict the break-up length of pressure-modulated slender capillary jets.

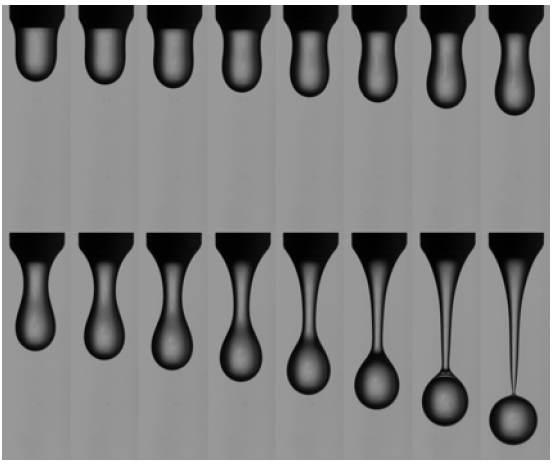

Figure 1.5: Sequence of images showing the evolution of a pendant drop of PDMS silicone oil of viscosity $\nu = 20$ cSt, injected at a constant flow rate $Q = 11$ ml/min through a tube of radius $R = 2$ mm. The time interval between two consecutive frames is 1/250 s.

1.2 Drops

However, the stretching effect of gravity acting on a vertically orientated fluid column is only relevant when the flow rate is above the jetting threshold mentioned in the previous section. In fact, if the liquid flow rate is not sufficiently large, a jet is not formed but, instead, drops with diameters similar to that of the injector, are emitted from the tube exit, being this the signature of the so called 'dripping regime'. As an example, Figure 1.5 shows the evolution of a pendant drop of polydimethylsiloxane (PDMS) oil, issuing from a tube at a constant flow rate.

Millimetric drops are routinely used for the characterization of fluid-fluid interfaces. For instance, in the drop weight method, the static equilibrium between surface tension forces and the weight of a pendant liquid drop allows to extract the surface tension coefficient. The requirement of a small flow rate to avoid dynamic effects could be a problem when the working fluid is volatile, but the development of one-dimensional models to describe the dynamics of drop formation avoids this limitation (Yildirim *et al.*, 2005).

In fact, in many practical applications, the inertia of the flow is not negligible, and its competition with the gravitational and surface tension forces may lead to chaotic behaviours, depending on the damping effect of the viscosity.

The simplest and most common example is a dripping faucet, which has been studied as a paradigm of chaotic system for many years (Shaw, 1984). For instance, Coullet *et al.* (2005) gave a hydrodynamical explanation for this chaotic behaviour through modelling and numerical simulations.

In addition, not only the process of drop formation prior to break-up is of interest, but also the subsequent dynamics after the pinch-off of a drop. For instance, the presence of undesired satellite droplets can be a problem in some applications where monodispersity is a strong requirement. Consequently, the dynamics of liquid ligaments has been thoroughly studied to provide insight about the number and sizes of droplets resulting from a fragmentation scenario (Villermaux, 2007). The problem was studied numerically by Notz & Basaran (2004), where a comparison of the results of one-dimensional and two-dimensional simulations is reported. Another relevant work is due to Marmottant & Villermaux (2004*a*), who performed experiments pulling water from a free surface with a rod, in a configuration similar to the liquid bridges that will be presented in the next section. The experiments of Castrejón-Pita *et al.* (2012) provided evidence for the conditions under which a recoiling liquid filament breaks up into one or multiple drops, for a wide range of the governing parameters, while Driessen *et al.* (2013) analysed the same configuration both analytically and by means of a numerical model. The phenomenon is of interest for the inkjet printing industry, and Hoath *et al.* (2013) extended the geometry of the liquid filament by adding a blob of liquid at one of the ends. The work by Hoepffner & Paré (2013) should be also mentioned, because of the description of a mechanism that may appear during the recoiling stage, namely an escape from the pinching through a creation of a vortex ring.

1.3 Liquid bridges

The lapping of cats and dogs when drinking (Reis *et al.*, 2010), the formation of solidified strands in volcanic eruptions (Villermaux, 2012), the generation of spray droplets (Marmottant & Villermaux, 2004*b*), and the characterization of rheological properties of fluids (McKinley, 2005) represent a variety of phenomena of great interest both for natural processes and technical applications. These phenomena, despite their disparity, share a common fundamental feature: the existence of a liquid bridge in air, under a strong axial stretching.

Liquids bridges have been widely studied in the past. From their equilibrium shapes reviewed by Meseguer *et al.* (1999) to the dynamics of non-cylindrical,

axisymmetric, nearly unstable bridges studied by Perales & Vega (2011) under microgravity conditions.

The problem of a stretching liquid bridge originally received relatively little attention compared to their static shapes and oscillations. Kroger & Rath (1995) performed experiments using tracer particles to determine the elongation rates inside the bridge, and Gaudet *et al.* (1994) used the boundary integral method in the limit of Stokes flow to determine numerically the deformation of Newtonian liquid bridges without break-up, as the previous step to the design of the pioneering experiments that today allow to measure the extensional viscosity of non-Newtonian fluids (McKinley & Sridhar, 2002).

Later on, Zhang *et al.* (1996) provided a quantitative account of the effect of the liquid properties and the geometry on the non-linear deformation and break-up of stretching liquid bridges, by means of experiments and numerical simulations. The effect of both soluble (Liao *et al.*, 2004) and insoluble surfactants (Liao *et al.*, 2006) on the problem was also studied by Prof. Basaran's group.

Liquid bridges are commonly used as a model to characterize the detachment of pendant drops. For instance, the released drop size at very low flow rates is directly related to the stability of stretching capillary bridges (see e.g. Eggers, 1997).

In the last years, the configuration has attracted a lot of attention along several areas unsufficiently investigated. For instance, Vincent *et al.* (2014*b*) studied the remnants after a fast withdrawal; the early-time forced dynamics in the viscous case was described by means of an asymptotic analysis by Vincent *et al.* (2014*a*); the dynamics of liquid bridges close to the minimum-volume stability was studied both experimentally and numerically by Vega *et al.* (2014), and Duchemin *et al.* (2015) derived a self-similar solution for the impulse response in the inviscid case.

The most prominent example of the use of a liquid bridge as a model system to characterize the thinning and break-up of filaments is the Capillary Breakup Extensional Rheometer, CaBER. A sample of liquid is held between two rods, that are pulled apart to create a slender unstable filament whose temporal evolution allows to extract material properties of the fluid, such as the extensional viscosity (McKinley & Tripathi, 2000), or the relaxation time in case of viscoelastic fluids. An example of a CaBER experiment with glycerol as a sample liquid is shown in Figure 1.6.

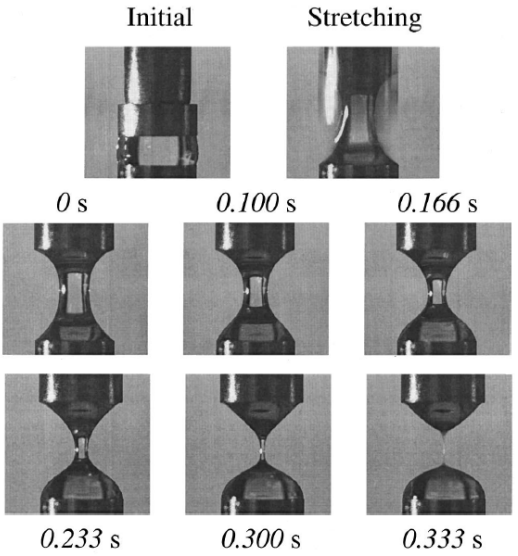

Figure 1.6: Sequence of images showing the initial configuration and extensional deformation of a viscous glycerol filament followed by the onset of viscocapillary drainage leading to break-up in a CaBER experiment. Adapted from McKinley & Tripathi (2000).

1.4 Complex fluids

In all the configurations presented up to this point, the liquid properties are crucial to determine the flow characteristics. Indeed, many of the fluids used in applications such as inkjet printing, spraying, or dispensing operations in the alimentary or pharmaceutical industries often exhibit a complex rheological behaviour (Chen, 2009). Thus, an operation as simple as the accurate dosing of a liquid can be a problem depending on the fluid properties (Clasen *et al.*, 2012).

The strain-stress relationship associated with non-Newtonian fluids is a source of complex behaviour. As an example, the differences between Newtonian and shear thinning fluids in a stretching liquid bridge was studied numerically by Yildirim & Basaran (2001), showing that the dynamics may be substantially modified when considering even the most simple generalized Newtonian fluid.

Another relevant aspect of the fluid is its possible viscoelastic behaviour. In fact, fluids used in fiber spinning applications often contain long entangled

Figure 1.7: Sequence of images showing the 'gobbling' phenomenon: a large terminal drop periodically develops at the end of a thin jet of a viscoelastic fluid. From Clasen *et al.* (2009).

polymeric chains that, when stretched, are capable of ravelling out and recover later, thus adding elasticity to the material properties. This viscoelastic behaviour can be found in many liquids, some of them as familiar as saliva. The phenomenon of beads on a string studied by Bhat *et al.* (2010) is a consequence of the interplay of viscosity, inertia, capillarity and elasticity in the thinning and break-up of filaments. Another example of how the elastic recovery modifies the dynamics of the jetting to dripping transition can be found in Clasen *et al.* (2009), where the existence of large drops of size much greater than the injector diameter attached at the tip of the jet is reported and explained. Figure 1.7 depicts an example of the latter phenomena, called 'gobbling'.

In addition, the presence of solid particles in a viscous liquid is another example of complex fluid. Suspensions are ubiquitous in nature and industry, with many different examples such as blood, paints and waste slurries. Inks used in daylife printing operations contain solid particles that can modify the normal dripping and jetting response (Basaran *et al.*, 2013) and every novel printing application recently developed or in progress has to deal with the jetting of suspensions (Hoath *et al.*, 2014).

1.5 Outline of the dissertation

The present dissertation can be summarized as follows. In Chapter 2 the critical flow rate for which a free falling liquid jet is no longer steady, namely, the flow rate for which the jetting to dripping transition takes place is determined. More

precisely, the range of liquid viscosities as well as the injection nozzle diameters explored by Sauter & Buggisch (2005) have been increased, finding that the experimental measurements are in strong disagreement with their theoretical predictions, a fact that motivates to revisit their analysis. The main conclusion drawn from Chapter 2 is that the one-dimensional equations by García & Castellanos (1994) and Eggers & Dupont (1994), which retain the expression for the full curvature in the formulation, are able to accurately predict not only the critical flow rate for which the jetting to dripping transition takes place but also the frequency of the self-sustained oscillations experienced by the jet at the critical conditions.

Chapter 3 deals with the non-linearity of the dripping regime, extending the works of Ambravaneswaran *et al.* (2004) and Subramani *et al.* (2006) on the complex response of a dripping faucet. Specifically, the range of injector sizes has been increased, showing that the previous scaling laws for the jetting transition fail when considering injector radii larger than those previously studied. In addition, new phase diagrams are depicted in regions of the parameter space not explored before, finding new regimes with the presence of satellite drops which had not been reported up to date.

In Chapter 4 the drop formation of dilute particulate suspensions in a Newtonian matrix is studied by investigating the thinning dynamics of a liquid bridge. The work of McIlroy & Harlen (2014) is extended to describe the final stage before break-up of a suspension, which occurs in a liquid thread between two confining beads. The model, based on the one-dimensional mass and momentum conservation equations, shows quantitative agreement with the experimentally observed deceleration and final pinching behaviour of the medium between individually monitored particles in the suspension (Mathues *et al.*, 2015).

Finally, the conclusions of this Ph.D. Thesis are summarized in Chapter 5 together with the future prospects.

References

Ambravaneswaran, B., Subramani, H. J., Phillips, S. D. & Basaran, O. A. 2004 Dripping-jetting transitions in a dripping faucet. *Phys. Rev. Lett.* 93, 034501.

Barrero, A. & Loscertales, I. G. 2007 Micro- and nanoparticles via capillary flows. *Annu. Rev. Fluid Mech.* 39, 89–106.

Basaran, O. A., Gao, H. J. & Bhat, P. P. 2013 Nonstandard inkjets. *Annu. Rev. Fluid Mech.* 45, 85–113.

Bhat, P. P., Appathurai, S., Harris, M. T., Pasquali, M., McKinley, G. H. & Basaran, O. A. 2010 Formation of beads-on-a-string structures during break-up of viscoelastic filaments. *Nature* 6, 625–631.

Castrejón-Pita, A. A., Castrejón-Pita, J. R. & Hutchings, I. M. 2012 Breakup of liquid filaments. *Phys. Rev. Lett.* 108, 074506.

Chen, X. B. 2009 Modeling and control of fluid dispensing prprocess: A state of the art review. *Int. J. Adv. Manuf. Technol.* 43, 276–286.

Clasen, C., Bico, J., Entov, V. M. & McKinley, G. H. 2009 'Gobbling drops': the jetting–dripping transition in flows of polymer solutions. *J. Fluid Mech.* 636, 5–40.

Clasen, C., Phillips, P. M., Palangetic, L. & Vermant, J. 2012 Dispensing of rheologically complex fluids: The map of misery. *AIChE J.* 58, 3242–3255.

Consoli-Lizzi, P., Coenen, W. & Sevilla, A. 2014 Experiments and non-parallel theory on the natural break-up of freely falling newtonian liquid jets. In *Bulletin of the American Physical Society*, , vol. 59, pp. 244–245.

Coullet, P., Mahadevan, L. & Riera, C. S. 2005 Hydrodynamical models for the chaotic dripping faucet. *J. Fluid Mech.* 526, 1–17.

Denn, M. M. 1980 Continuous drawing of liquids to form fibers. *Annu. Rev. Fluid Mech.* 12, 365–387.

Doshi, J. & Reneker, D. H. 1995 Electrospinning process and applications of electrospun fibers. *J. Electrostatics* 35, 151–160.

Driessen, T., Jeurissen, R., Wijshoff, H., Toschi, F. & Loshe, D. 2013 Stability of viscous long liquid filaments. *Phys. Fluids* 25, 062109.

Duchemin, L., Dizès, S. Le, Vincent, L. & Villermaux, E. 2015 Self-similar impulsive capillary waves on a ligament. *Phys. Fluids* 27, 051704.

Eggers, J 1997 Nonlinear dynamics and breakup of free surface flows. *Rev. Mod. Phys.* 69, 865–929.

Eggers, J. & Dupont, T. F. 1994 Drop formation in a one-dimensional approximation of the navier-stokes equation. *J. Fluid Mech.* 262, 205–222.

Eggers, J. & Villermaux, E. 2008 Physics of liquid jets. *Rep. Prog. Phys.* 71, 036601.

Gañán-Calvo, A. M. 1998 Generation of steady liquid microthreads and micron-sized monodisperse sprays in gas streams. *Phys. Rev. Lett.* 80 (2), 285–288.

García, F. J. & Castellanos, A. 1994 One-dimensional models for slender axisymmetric viscous liquid jets. *Phys. Fluids* 6 (8), 2676–2689.

García, F. J., González, H., Castrejón-Pita, J. R. & Castrejón-Pita, A. A. 2014 The breakup length of harmonically stimulated capillary jets. *Appl. Phys. Lett.* 105, 094104.

Gaudet, S., McKinley, G. H. & Stone, H. A. 1994 Extensional deformation on newtonian and non-newtonian liquid bridges in microgravity. *AIAA* 94, 1–9.

Gordillo, J. M., Sevilla, A. & Campo-Cortés, F. 2014 Global stability of stretched jets: conditions for the generation of monodisperse micro-emulsions using coflows. *J. Fluid Mech.* 738, 335–357.

Hoath, S. D., Hsiao, W. K., Hutchings, I. M. & Tuladhar, T. R. 2014 Jetted mixtures of particle suspensions and resins. *Phys. Fluids* 26, 101701.

Hoath, S. D., Jung, S. & Hutchings, I. M. 2013 A simple criterion for filament break-up in drop-on-demand inkjet printing. *Phys. Fluids* 25, 021701.

Hoepffner, J. & Paré, G. 2013 Recoil of a liquid filament: escape from pinch-off through creation of a vortex ring. *J. Fluid Mech.* 734, 183–197.

Kroger, R. & Rath, H. J. 1995 Velocity and elongation rate distributions in stretched polymeric and newtonian liquid bridges. *J. Non-Newtonian Fluid Mech.* 57, 137–153.

Liao, Y. C., Franses, E. I. & Basaran, O. A. 2006 Deformation and breakup of a stretching liquid bridge covered with an insoluble surfactant monolayer. *Phys. Fluids* 18, 022101.

Liao, Y. C., Subramani, H. J., Franses, E. I. & Basaran, O. A. 2004 Effects of soluble surfactants on the deformation and breakup of stretching liquid bridges. *Lagmuir* 20, 9926–9930.

Loscertales, I. G., Barrero, A., Guerrero, I., Cortijo, R., Marquez, M. & Gañán-Calvo, A. M. 2002 Micro/nano encapsulation via electrified coaxial liquid jets. *Science* 295, 1695–1698.

Marín, A. G., Campo-Cortés, F. & Gordillo, J. M. 2009 Generation of micron-sized drops and bubbles through viscous coflows. *Colloid Surface A* 344, 2–7.

Marín, A. G., Loscertales, I. G., Marquez, M. & Barrero, A. 2007 Simple and double emulsions via coaxial jet electrosprays. *Phys. Rev. Lett.* 98, 014502.

Marmottant, P. & Villermaux, E. 2004*a* Fragmentation of stretched liquid ligaments. *Phys. Fluids* 16, 2732.

Marmottant, P. & Villermaux, E. 2004*b* On spray formation. *J. Fluid Mech.* 498, 73–111.

Mathues, W., McIlroy, C., Harlen, O. G. & Clasen, C. 2015 Capillary breakup of suspensions near pinch-off. *Phys. Fluids* 27, 093301.

McIlroy, C. & Harlen, O. G. 2014 Modelling capillary breakup of particulate suspensions. *Phys. Fluids* 26, 033101.

McKinley, G. H. 2005 Visco-elasto-capillary thinning and break-up of complex fluids. *Rheol. Rev.* 3, 1–48.

McKinley, G. H. & Sridhar, T. 2002 Filament-stretching rheometry of complex fluids. *Annu. Rev. Fluid Mech.* 34, 375–415.

McKinley, G. H. & Tripathi, A. 2000 How to extract the Newtonian visosity from Capillary Breakup Measurements in a filament rheometer. *J. Rheol.* 44, 653–671.

Meseguer, J., Perales, J. M., Martínez, I. & Sanz, N. A. Bezdenejnykh A. 1999 'Hydrostatic instabilities' in floating zone crystal growth process. *Curr. Top. Cryst. Growth Res.* 5, 27–42.

Montanero, J. M., Herrada, M. A., Ferrera, C., Vega, E. J. & Gañán-Calvo, A. M. 2011 On the validity of a universal solution of viscous capillary jets. *Phys. Fluids* 23, 122103.

Notz, P. K. & Basaran, O. A. 2004 Dynamics and breakup of a contracting liquid filament. *J. Fluid Mech.* 512, 223–256.

Pearson, J. R. A. & Matovich, M. A. 1969 Spinning a molten threadline. *I&EC fundamentals* 8, 605–609.

Perales, J. M. & Vega, J. M. 2011 Dynamics of nearly unstable axisymmetric liquid bridges. *Phys. Fluids* 23, 012107.

Reis, P. M., Jung, S., Aristoff, J. M. & Stocker, R. 2010 How cats lap: Water uptake by Felix catus. *Science* 330, 1231–1234.

Rodríguez-Rodríguez, J., Sevilla, A., Martínez-Bazán, C. & Gordillo, J. M. 2015 Generation of microbubbles with applications to industry and medicine. *Annu. Rev. Fluid Mech.* 47, 405–429.

Sauter, U. S. & Buggisch, H. W. 2005 Stability of initially slow viscous jets driven by gravity. *J. Fluid Mech.* 533, 237–257.

Shaw, R. 1984 *The dripping faucet as a model chaotic system*. Santa Cruz, CA: Aerial Press.

Stokes, Y. M., Buchak, P., Crowdy, D. G. & Ebendorff-Heidepriem, H. 2014 Drawing of micro-structured fibres: circular and non-circular tubes. *J. Fluid Mech.* 755, 176–203.

Subramani, H. J., Yeoh, H. K., Suryo, R., Xum, Q., Ambravaneswaran, B. & Basaran, O. A. 2006 Simplicity and complexity in a dripping faucet. *Phys. Fluids* 18, 032106.

Suñol, F. & González-Cinca, R. 2015 Liquid jet breakup and subsequent droplet dynamics under normal gravity and in microgravity conditions. *Phys. Fluids* 27, 077102.

Vega, E. J., Montanero, J. M., Herrada, M. A. & Ferrera, C. 2014 Dynamics of an axisymmetric liquid bridge close to the minimum-volume stability limit. *Phys. Rev. E* 90, 013015.

Villermaux, E. 2007 Fragmentation. *Annu. Rev. Fluid Mech.* 39, 419–446.

Villermaux, E. 2012 The formation of filament structures from molten silicates: Pele's hair, angel hair, and blown clinker. *C. R. Mecanique* 340, 555–564.

Vincent, L., Duchemin, L. & Le Dizès, S. 2014*a* Forced dynamics of a short viscous liquid bridge. *J. Fluid Mech.* 761, 220–240.

Vincent, L., Duchemin, L. & Villermaux, E. 2014*b* Remnants from fast liquid withdrawal. *Phys. Fluids* 26, 031701.

Yildirim, O. E. & Basaran, O. A. 2001 Deformation and breakup of stretching bridges of newtonian and shear-thinning liquids: comparison of one- and two-dimensional models. *Chem. Eng. Sci.* 56, 211–233.

Yildirim, O. E., Xu, Q. & Basaran, O. A. 2005 Analysis of the drop weight method. *Phys. Fluids* 17, 062107.

Zhang, X., Padgett, R. S. & Basaran, O. A. 1996 Nonlinear deformation and breakup of stretching liquid bridges. *J. Fluid Mech.* 329, 207–245.

CHAPTER
TWO

Shape and stability of gravitationally stretched jets

Contents

2.1 Introduction

The purpose in this chapter is to find both from an experimental and a theoretical point of view the critical flow rate Q_c determining the transition from jetting to dripping, not the boundary for which the inverse transition, i.e, from dripping to jetting, takes place. Indeed, Clanet & Lasheras (1999) reported that Q_c presents a hysteretic behaviour since the value of the critical flow rate for which an initially long jet disappears as a consequence of slowly decreasing the injected flow rate, i.e. the transition from jetting to dripping, is smaller than the critical value for which a long jet is formed when the flow rate is slowly increased starting from a situation in which drops are emitted directly from the tube exit, i.e. the transition from dripping to jetting. Notice that the minimum

achievable drop size decreases with the critical flow rate for a given fluid and injector size and that our purpose here is to envisage an alternative method to reduce as much as possible the size of the fluid filaments generated from a given nozzle by means of gravitational acceleration. These reasons, together with the hysteretic behaviour of the critical flow rate described above, justify the focus put here on the study of the transition from jetting to dripping, not on the reverse situation.

To characterize the transition from jetting to dripping from a purely theoretical point of view, Leib & Goldstein (1986) analysed the growth and propagation of capillary perturbations on a purely cylindrical jet. These authors found that, for a given liquid and nozzle exit diameter, there exists a critical flow rate below which the spatial analysis (Keller *et al.*, 1972; Guerrero *et al.*, 2012) is not well posed since the flow is absolutely unstable (Landau, 1946; Briggs, 1964; Huerre & Monkewitz, 1985) i.e., the perturbations grow in time without propagating and the jet formation process is thus inhibited. Nevertheless, the theoretically determined boundary separating the region where the jet is absolutely unstable from that in which it is convectively unstable, is only in order of magnitude agreement with the experimentally determined critical conditions for which the jetting to dripping transition takes place. This is due to the fact that the type of analysis that rests on the parallel flow assumption can only be applied to flows that are weakly non-parallel at the wavelength of the unstable mode and so, in cases like that shown in Figure 1.4, where a highly stretched jet is depicted, the use of classical parallel stability theory is, at least, questionable.

To overcome the limitations associated with local stability theory, several studies have taken into account both global and non-parallel effects in the analysis. In particular, Schulkes (1994) performed a numerical study of drop formation under the assumption of ideal flow, obtaining a dripping-jetting transition when the injected flow rate exceeds a critical value that depends on the size of the injector. For slender jets in which the inertial effects are dominant over gravity forces, Le Dizès (1997) extended the work of Leib & Goldstein (1986), showing that a global instability prevents the formation of the jet for small enough exit velocities and Senchenko & Bohr (2005) used multiple scale analysis to show the stabilizing effect of gravitational acceleration in the growth of capillary perturbations. Unfortunately, the stability theory of Le Dizès (1997), which is the first to account for weakly non parallel effects, does not predict the experimental observations of Clanet & Lasheras (1999), but Sevilla (2011) showed that the agreement between the spatiotemporal stability theory and

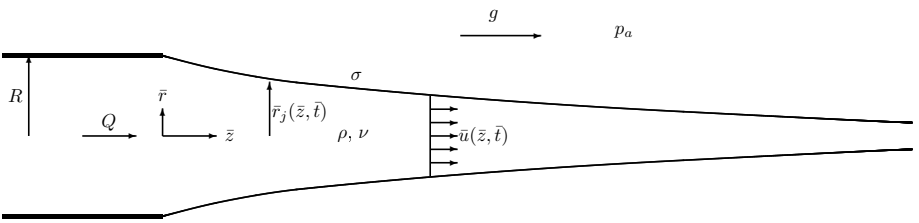

Figure 2.1: Sketch of the problem and the physical parameters involved in the model.

experiments notably improves if viscous relaxation effects are taken into account. Finally, of special interest for the purposes of the present investigation is the study by Sauter & Buggisch (2005), who theoretically and experimentally analysed the global stability of very viscous jets ($\nu > 10^{-3}$ m^2/s) stretched by gravity. In their work, Sauter & Buggisch (2005) were the first to describe a linear global mode which represents self-sustained oscillations of the jet and, in addition, calculated the critical flow rate at which this oscillating mode is experimentally observed.

2.2 Problem statement

The conceptual definition of the problem is simple. Consider a Newtonian liquid of density ρ, and kinematic viscosity ν. This liquid is injected into stagnant air in the presence of a gravitational acceleration g, being σ the corresponding liquid-air surface tension coefficient. The surrounding gaseous atmosphere is considered to be at ambient pressure p_a, and the injection takes place through a cylindrical injector of radius R at a constant flow rate Q, as depicted in Figure 2.1.

2.2.1 Experimental setup

The experimental setup consists of a vertically oriented capillary tube of radius R through which different PDMS silicone oils from Sigma-Aldrich, whose properties are summarized in Table 2.1, are injected at a constant flow rate using a Harvard Apparatus PhD Ultra syringe pump. The jet images are recorded using a Red Lake Motion Pro X high speed camera. To avoid ambient disturbances, both the injector and the camera are installed inside a chamber placed on a vibration-isolation table. The liquid is supplied through either Sigma Aldrich

ν [mm^2 s^{-1}]	ρ [kg m^{-3}]	σ [mN m^{-1}]	Γ
50	960	20.8	0.84
100	965	20.9	1.67
200	970	21.1	3.33
350	970	21.1	5.83
1000	970	21.1	16.67

Table 2.1: Properties at 25°C of the used silicon oils, and their corresponding values of $\Gamma = 3\nu(\rho^3 g/\sigma^3)^{1/4}$, computed using a value of $g = 9.81$ ms^{-2}.

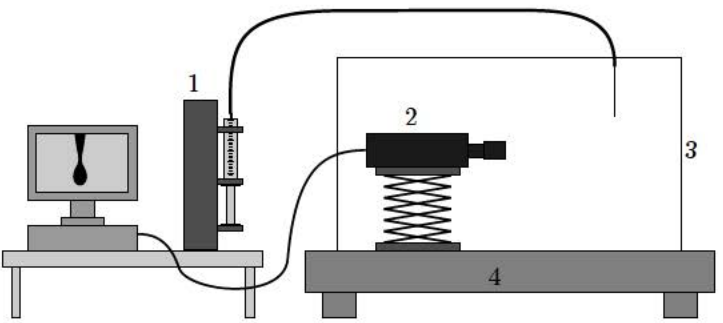

Figure 2.2: Sketch of the experimental facility. (1) Syringe pump, (2) high-speed camera, (3) insulation chamber and (4) vibration isolation table.

hypodermic needles or stainless steel tubes from Tubca. The outer radii of the capillary tubes range between 0.825 and 3.5 mm, and their length-to-diameter ratio is high enough to ensure a fully developed velocity profile at the needle exit. A sketch of the experimental setup is shown in Figure 2.2.

2.3 Mathematical model

To analyse the stability of gravitationally stretched axisymmetric jets like those shown in Figures 1.4 and 2.3, the dimensionless leading-order one-dimensional mass and momentum equations deduced by García & Castellanos (1994) and Eggers & Dupont (1994) are used. The jet is axisymmetric, with constant and uniform liquid properties and the effects of the surrounding gaseous atmosphere are negligible, since the density and viscosity of the gas are much smaller than

those of the liquid. Thus, the continuity equation writes,

$$\frac{\partial \bar{r}_j^2}{\partial \bar{t}} + \frac{\partial (\bar{r}_j^2 \bar{u})}{\partial \bar{z}} = 0, \tag{2.1}$$

while the momentum equation along the axial coordinate takes the form

$$\frac{\partial \bar{u}}{\partial \bar{t}} + \bar{u}\frac{\partial \bar{u}}{\partial \bar{z}} = -\frac{1}{\rho}\frac{\partial p}{\partial \bar{z}} + g + \frac{3\nu}{\bar{r}_j^2}\frac{\partial}{\partial \bar{z}}\left(\bar{r}_j^2 \frac{\partial \bar{u}}{\partial \bar{z}}\right), \tag{2.2}$$

where the dependent variables $\bar{u}$ and $\bar{r}_j$ are the liquid velocity and jet radius respectively, $\bar{z}$ is the axial coordinate and $\bar{t}$ is time.

In (2.2), p denotes the liquid pressure, which can be expressed as the sum of the ambient pressure plus the capillary pressure,

$$p = p_a + \sigma \bar{\mathcal{C}}, \tag{2.3}$$

where $\bar{\mathcal{C}}$ indicates the interfacial curvature

$$\bar{\mathcal{C}} = \bar{r}_j^{-1}\left[1 + \left(\frac{\partial \bar{r}_j}{\partial \bar{z}}\right)^2\right]^{-1/2} - \frac{\partial^2 \bar{r}_j}{\partial \bar{z}^2}\left[1 + \left(\frac{\partial \bar{r}_j}{\partial \bar{z}}\right)^2\right]^{-3/2}. \tag{2.4}$$

The choice of the leading-order momentum equation (2.2), over more precise higher-order one-dimensional descriptions like the parabolic model developed by García & Castellanos (1994), was due to the fact that (2.2) is the simplest approximation of the axial momentum equation that incorporates the main physical mechanisms involved in the global stability of the jetting regime, namely liquid inertia, as well as viscous, gravitational and surface tension forces.

The solution depends on the constant flow rate Q and on the size of the injector R through the boundary conditions at $\bar{z} = 0$:

$$\bar{r}_j(0, \bar{t}) = R, \tag{2.5}$$

$$\bar{u}(0, \bar{t}) = U, \tag{2.6}$$

being $U = Q/(\pi R^2)$ the mean velocity at the nozzle exit.

2.3.1 Dimensionless formulation

It proves convenient to carefully choose the characteristic scales used to non-dimensionalize the equations (2.1)-(2.2). The first attempt would be to consider the radius of the injector as the characteristic length scale $z_c = R$, and the mean outlet velocity as velocity scale, $u_c = U$. With this choice, the three non-dimensional parameters governing the problem would be the Reynolds number,

$Re = RU/\nu$, the Froude number, $Fr = U^2/(gR)$, and the Weber number, $We = \rho U^2 R/\sigma$, defined as usual.

The use of these scales would introduce the three non-dimensional parameters in the momentum equation (2.2), while the dimensionless boundary conditions at the outlet would be equal to one independently of the parameter values. Although this can be considered as an advantage, it turns out that the variations of some of the stability properties, like the non-dimensional eigenmode frequencies, span several orders of magnitude, thus suggesting that a better scaling for the flow variables, based on the physics of the problem, is clearly possible.

To that end, the proper characteristic scales have been found by balancing the different terms of the momentum equation (2.2). Note that the non-dimensionalization must take gravity into account, since it is the basic stretching mechanism in the flow under study, but keeping in mind that it is desirable to contemplate the inviscid limit as a regular one.

The order of magnitude of the different terms in (2.2) is

$$\bar{u}\frac{\partial \bar{u}}{\partial \bar{z}} \sim \frac{u_c^2}{z_c}, \tag{2.7}$$

$$\frac{1}{\rho}\frac{\partial p}{\partial \bar{z}} \sim \frac{\sigma \mathcal{C}}{\rho z_c} \sim \frac{\sigma}{\rho r_{j,c} z_c}, \tag{2.8}$$

where $r_{j,c}$ is the length scale for the jet radius, and it has been taken into account that the curvature $\mathcal{C} \sim r_{j,c}^{-1}$. It is reasonable to use only one length scale for both z and r_j for simplicity but also because the focus is on small values of the Weber number for which $\partial r_j/\partial z \sim \mathcal{O}(1)$. In addition, this choice improves the stability of the numerical method used to solve the problem, which will be explained in Section 2.4.

When the flow rate is small, as occurs when thin jets are desired close to the outlet, the Weber number is also small. Thus, the gravity and pressure gradient terms are in dominant balance near the exit, where the jet behaves as a static meniscus at leading order. In contrast, inertial effects become dominant over the surface tension terms sufficiently far downstream. Consequently, it is possible to balance the three mentioned terms,

$$\frac{u_c^2}{z_c} \sim \frac{\sigma}{\rho z_c^2} \sim g, \tag{2.9}$$

yielding the following characteristic scales

$$z_c = \left(\frac{\sigma}{\rho g}\right)^{1/2}, \tag{2.10}$$

$$u_c = \left(\frac{\sigma g}{\rho}\right)^{1/4}, \tag{2.11}$$

$$t_c = \frac{z_c}{u_c} = \left(\frac{\sigma}{\rho g^3}\right)^{1/4}. \tag{2.12}$$

The characteristic length scale for the problem is, thus, the capillary length l_σ, while the velocity scale is the free-fall velocity based on this length $\sqrt{g\,l_\sigma}$ (Senchenko & Bohr, 2005), and the variables in equations (2.1)-(2.4) can be made dimensionless using these scales, yielding

$$\frac{\partial r_j^2}{\partial t} + \frac{\partial (u r_j^2)}{\partial z} = 0, \tag{2.13}$$

$$\frac{\partial u}{\partial t} + u\frac{\partial u}{\partial z} = 1 - \frac{\partial \mathcal{C}}{\partial z} + \frac{\Gamma}{r_j^2}\frac{\partial}{\partial z}\left(r_j^2 \frac{\partial u}{\partial z}\right), \tag{2.14}$$

being $r_j = \bar{r}_j/l_\sigma$, $u = \bar{u}/\sqrt{g\,l_\sigma}$, $z = \bar{z}/l_\sigma$ and $t = \bar{t}/t_c$ the corresponding dimensionless variables.

Thus, the system (2.13)-(2.14) only depends on the Kapitza number Γ, defined as

$$\Gamma = 3\nu\left(\frac{\rho^3 g}{\sigma^3}\right)^{1/4}, \tag{2.15}$$

which is constant for a given liquid and a fixed value of the gravitational acceleration. The dimensionless version of the boundary conditions (2.5)-(2.6) reads:

$$r_j(0,t) = \frac{R}{l_\sigma} = Bo^{1/2}, \tag{2.16}$$

$$u(0,t) = \frac{U}{\sqrt{g\,l_\sigma}} = We^{1/2} Bo^{-1/4}, \tag{2.17}$$

where $Bo = \rho g R^2/\sigma$ is the Bond number.

2.3.2 Steady state

For globally stable jets like those shown in Figure 1.4, both the steady jet shape r_{j0} and the corresponding liquid velocity can be described making use of the steady solution of the continuity equation (2.13),

$$r_{j0}^2 u_0 = q \rightarrow u_0 = q/r_{j0}^2, \tag{2.18}$$

being $q = Bo^{3/4}We^{1/2}$ the dimensionless flow rate, and of the steady form of the momentum equation (2.14),

$$u_0 u_0' = 1 - \mathcal{C}_0' + \Gamma\, r_{j0}^{-2} \left(r_{j0}^2 u_0'\right)', \tag{2.19}$$

where primes denote derivatives with respect to z and $\mathcal{C}_0$ is the expression of the jet interfacial curvature when r_j is replaced by r_{j0} in the dimensionless version of equation (2.4). The substitution of the equation for u_0 given in (2.18) into (2.19) provides the following equation for r_{j0},

$$-r_{j0}^2\mathcal{C}_0' + 2q\Gamma\left[r_{j0}^{-2}\left(r_{j0}'\right)^2 - r_{j0}^{-1}r_{j0}''\right] + 2q^2 r_{j0}^{-3} r_{j0}' + r_{j0}^2 = 0, \tag{2.20}$$

which needs to be solved subjected to the steady counterpart of the boundary condition (2.16),

$$r_{j0}(z=0) = Bo^{1/2}. \tag{2.21}$$

In equation (2.20), notice that the term associated to the capillary pressure gradient writes

$$-r_{j0}^2\mathcal{C}_0' = \frac{r_{j0}'}{\left[1+\left(r_{j0}'\right)^2\right]^{1/2}} + \frac{r_{j0}r_{j0}'r_{j0}'' + r_{j0}^2 r_{j0}'''}{\left[1+\left(r_{j0}'\right)^2\right]^{3/2}} - \frac{3r_{j0}^2 r_{j0}'\left(r_{j0}''\right)^2}{\left[1+\left(r_{j0}'\right)^2\right]^{5/2}}. \tag{2.22}$$

2.3.3 Linear stability

To find the critical conditions at which the jetting to dripping transition takes place, it is necessary to determine whether the solutions to equations (2.20)-(2.22) are stable or sustain the self-excited oscillations. To that end, solutions to the system (2.13)-(2.14) of the form

$$r_j(z,t) = r_{j0}(z) + \varepsilon\, r_{j1}(z)\, \mathrm{e}^{\omega t}, \tag{2.23}$$

$$u(z,t) = u_0(z) + \varepsilon\, u_1(z)\, \mathrm{e}^{\omega t}, \tag{2.24}$$

are sought for, where $\varepsilon \ll 1$, ω is an eigenfrequency, and $r_{j1}(z)$, $u_1(z)$ denote the corresponding eigenfunctions. Therefore, the steady solution will be stable if $\omega_r < 0$, and will be unstable provided that $\omega_r \geq 0$, with $\omega_r = \mathcal{R}(\omega)$ and $\mathcal{R}$ denoting the real part. Notice also that $\omega_i = \mathcal{I}(\omega)$ represents the oscillation frequency of the normal mode, being $\mathcal{I}$ the imaginary part. Substituting the Ansatz (2.23)-(2.24) into equations (2.13)-(2.14), and retaining the terms proportional to ε, yields the following system for the eigenvalues ω,

$$\begin{bmatrix} \mathcal{M}_r^c & \mathcal{M}_u^c \\ \mathcal{M}_r^m & \mathcal{M}_u^m \end{bmatrix} \begin{bmatrix} r_{j1} \\ u_1 \end{bmatrix} = \omega \begin{bmatrix} r_{j1} \\ u_1 \end{bmatrix}, \tag{2.25}$$

with $\mathcal{M}_i^j$ denoting the following differential operators,

$$\mathcal{M}_r^c = -\frac{q}{r_{j0}^2}\,\mathrm{D} + \frac{q\,r'_{j0}}{r_{j0}^3}\,\mathrm{I}\,, \tag{2.26}$$

$$\mathcal{M}_u^c = -\frac{r_{j0}}{2}\,\mathrm{D} - r'_{j0}\,\mathrm{I}\,, \tag{2.27}$$

$$\mathcal{M}_r^m = \sum_{k=1}^{4} s^{2k-1}\,\mathcal{T}_k - 4\Gamma q\left(\frac{r'_{j0}}{r_{j0}^4}\,\mathrm{D} - \frac{\left(r'_{j0}\right)^2}{r_{j0}^5}\,\mathrm{I}\right)\,, \tag{2.28}$$

$$\mathcal{M}_u^m = \Gamma\left(\mathrm{D}^2 + \frac{2r'_{j0}}{r_{j0}}\,\mathrm{D}\right) - \frac{q}{r_{j0}^2}\,\mathrm{D} + \frac{2q\,r'_{j0}}{r_{j0}^3}\,\mathrm{I}\,. \tag{2.29}$$

In (2.26)-(2.29), I is the identity operator, $\mathrm{D}^n \equiv \mathrm{d}^n/\mathrm{d}z^n$, $s(z) = [1+(r'_{j0})^2]^{-1/2}$ and

$$\mathcal{T}_1 = \frac{1}{r_{j0}^2}\,\mathrm{D} - \frac{2r'_{j0}}{r_{j0}^3}\,\mathrm{I}, \tag{2.30}$$

$$\mathcal{T}_2 = \mathrm{D}^3 + \frac{r'_{j0}}{r_{j0}}\,\mathrm{D}^2 - \left[\frac{\left(r'_{j0}\right)^2}{r_{j0}^2} - \frac{r''_{j0}}{r_{j0}}\right]\mathrm{D} - \frac{r'_{j0}\,r''_{j0}}{r_{j0}^2}\,\mathrm{I}, \tag{2.31}$$

$$\mathcal{T}_3 = -6\,r'_{j0}\,r''_{j0}\,\mathrm{D}^2 - 3\left[\frac{\left(r'_{j0}\right)^2 r''_{j0}}{r_{j0}} + \left(r''_{j0}\right)^2 + r'_{j0}\,r'''_{j0}\right]\mathrm{D}, \tag{2.32}$$

$$\mathcal{T}_4 = 15\left(r''_{j0}\right)^2\left(r'_{j0}\right)^2\,\mathrm{D}. \tag{2.33}$$

2.4 Numerical procedure

To solve both equation (2.20) for r_{j0}, and the system (2.25) for the eigenvalues ω, the corresponding differential operators are discretized using a Chebyshev collocation method (Canuto *et al.*, 2006). To that end, the physical domain, $0 \leq z \leq L$ is mapped into the interval $-1 \leq y \leq 1$ by means of the transformation

$$z = \frac{bL(1+y)}{2b + L(1-y)}, \tag{2.34}$$

where b is a parameter that controls the clustering of nodes at $z = 0$ and $z = L$. Derivatives with respect to z are calculated using the standard Chebyshev differentiation matrices and the chain rule (see Appendix A for details). The non-linear differential equation (2.20) is solved first using an iterative Newton-Raphson method. Once r_{j0} is known at the N Chebyshev collocation points, the discretized version of (2.25), which results in a linear algebraic eigenvalue problem to determine the $2N$ eigenvalues ω^k, $k = 1 \ldots 2N$, and their corresponding eigenfunctions (r_{j1}^k, u_1^k) at the N collocation points, is solved using

standard Matlab® routines. Notice that the eigenfunctions must accomplish $r_{j1}(z=0) = u_1(z=0) = 0$, and that there is no need to impose additional boundary conditions at $z = L$. This is due to the fact that the numerical method naturally converges, in the limit $z \to \infty$, to the most regular asymptotic solution of equation (2.20), namely $r_{j0} \to q^{1/2}(2z)^{-1/4}$, and to that of equation (2.25). Although all the results reported in the present chapter were computed with values of L, N and b within the ranges $100 \leq L \leq 150$, $100 \leq N \leq 200$ and $20 \leq b \leq 80$, it has been carefully checked that the leading eigenvalues and eigenfunctions are insensitive to the values of these parameters. Several tests have been also performed using the Neumann boundary conditions at $z = L$ chosen by Sauter & Buggisch (2005), namely $\mathrm{D}u_0(L) = 0$ for the steady flow and $\mathrm{D}u_1(L) = 0$ for the disturbance, giving identical results for large enough values of L.

2.5 Comparison with experiments

Figure 2.3 compares the solution $r_{j0}(z)$ of equation (2.20) obtained for different values of the control parameters (Γ, Bo, We) with their corresponding experimental images. As an example of the accuracy of the model, the maximum relative deviation between the theoretical and the experimental jet profile in Figure 2.3(b) is less than 1.85%. It should be pointed out that the almost perfect match between theory and experiments shown in Figure 2.3 has no free parameters, what constitutes the first evidence supporting the present analysis. It is also important to emphasize that the agreement is lost if the expression for the interfacial curvature given in (2.4) is substituted by its slender approximation, $\mathcal{C}_0 \simeq 1/r_{j0}$, as was done e.g. in Sauter & Buggisch (2005).

Once the steady shape of the jet is calculated for arbitrary values of the control parameters, the spectrum of eigenvalues and their corresponding eigenfunctions is calculated following the method described in Sections 2.3 and 2.4. Figure 2.4 shows the results obtained for $\Gamma = 5.83$, $Bo = 1.8$ and two different values of We. In Figures 2.4(a–c), in which the value of the Weber number is $We = 8 \times 10^{-3}$, the jet is stable since $\max(\omega_r^k) < 0$, while in Figures 2.4(d–f), where $We = 3 \times 10^{-3}$, the jet is unstable as the real part of the leading eigenvalue is slightly positive. From the results of Figure 2.4 it is deduced that the dominant eigenmode of the jet, firstly described by Sauter & Buggisch (2005), represents an oscillation of the liquid column of wavelength much larger than the nozzle radius. Notice also from Figure 2.4 that the wavelength grows down-

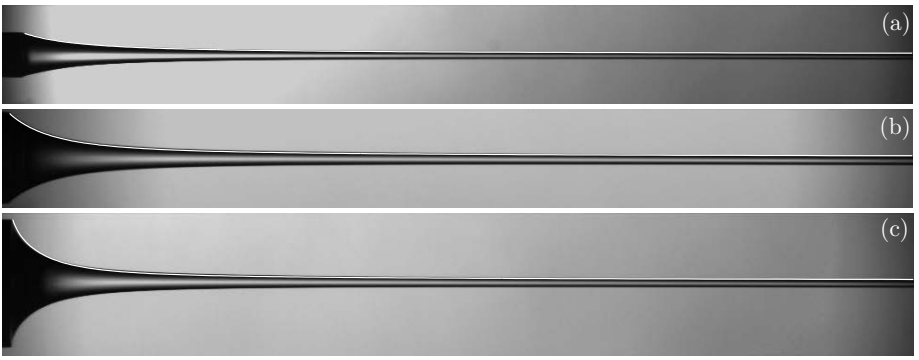

Figure 2.3: Comparison of the steady solution given by equation (2.20) with experiments for $\Gamma = 5.83$, $Bo = 0.71$, $We = 2.62 \times 10^{-2}$ (a), $\Gamma = 1.67$, $Bo = 1.81$, $We = 6.06 \times 10^{-3}$ (b) and $\Gamma = 3.33$, $Bo = 5.53$, $We = 1.85 \times 10^{-3}$ (c).

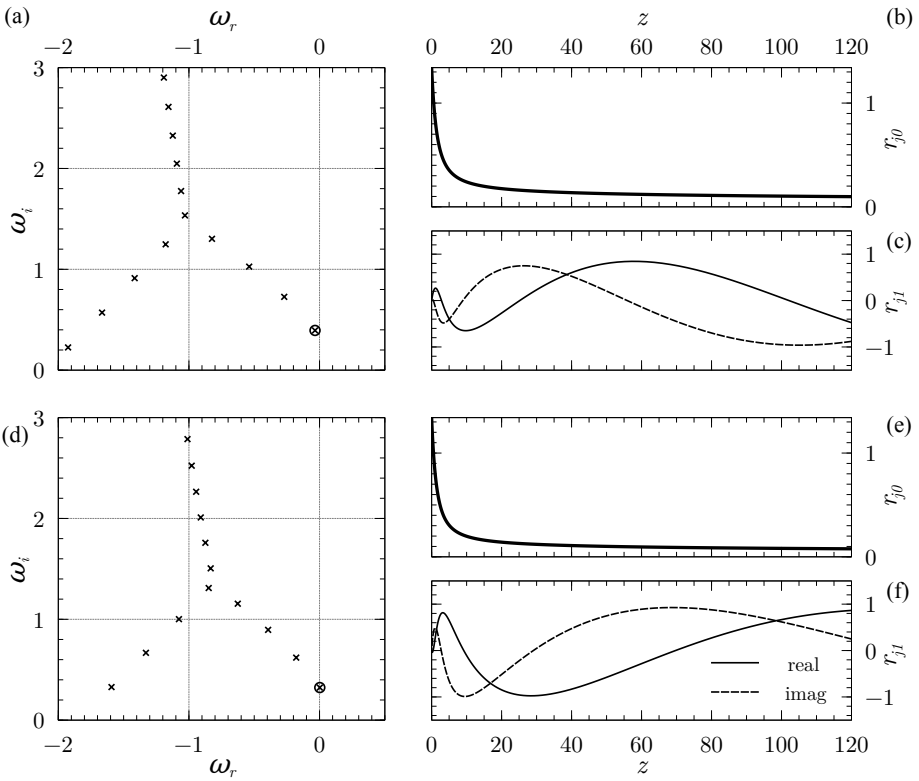

Figure 2.4: Spectrum of eigenvalues ω, steady shape of the jet, $r_{j0}(z)$, and real and imaginary parts of the leading eigenfunction for $\Gamma = 5.83$, $Bo = 1.8$ and two different values of We: in (a–c) $We = 8 \times 10^{-3}$ (stable case), and in (d-f) $We = 3 \times 10^{-3}$ (unstable case). The leading eigenvalue in (a) and (d) is enclosed with a circle.

stream as a consequence of the liquid acceleration, an effect already described by Tomotika (1936) and Frankel & Weihs (1985). Figure 2.4 also reveals that, since near the outlet the leading global mode evolves on a length scale larger than that associated to the variations of the steady jet, the classical parallel stability analysis based on local wavetrains cannot be used to correctly predict the global stability of the flow.

To check the validity of the global stability theory derived herein, the critical flow rate below which the jet experiences unsteady oscillations has been experimentally determined for each of the liquids and nozzles used. The jet was initially generated imposing a constant flow rate Q above the critical one, Q_c, and then Q was smoothly reduced to new constant values. If the jet remains stable, this process was repeated decreasing the final flow rate in 0.1 ml/min, until the self-excited oscillations were firstly observed, what fixed the value of Q_c and the corresponding value of the critical Weber number, We_c. In addition, the frequency of the oscillations was also measured from the analysis of the videos recorded at $Q = Q_c$. Figure 2.5(a) shows the measured values of the critical Weber number for the particular case of $\Gamma = 5.83$ and different values of the Bond number within the range $0.33 \leq Bo \leq 5.53$, together with several theoretical transition curves. The result of Sauter & Buggisch (2005), which reads

$$We_c^{\mathrm{SB}} = 0.0529\,\Gamma^{-0.396} Bo^{-0.297} \tag{2.35}$$

when expressed in terms of the dimensionless variables used here, is well above the experimental measurements. This evidence indicates that real jets are stable for flow rates substantially smaller than those predicted by Sauter & Buggisch (2005). The mismatch between their theoretical result and experiments is due to the fact that these authors approximate the interfacial curvature by its slender approximation $\mathcal{C} \simeq r_j^{-1}$. Indeed, as can be appreciated in Figure 2.5, the theoretical transition curve closely follows the experimental points for $Bo \gtrsim 1$, whereas it reproduces the results in Sauter & Buggisch (2005) when the expression for the full curvature given in (2.4) is substituted by $\mathcal{C} \simeq r_j^{-1}$. This conclusion highlights the essential role played by the axial curvature in stabilizing the jet, as was already pointed out by Plateau (1873) and Rayleigh (1878). This stabilizing effect is especially relevant for large values of Bo, i.e. when the jet is highly stretched downstream. Notice also from Figure 2.5(b) that the frequencies of oscillation measured at the critical conditions are accurately predicted by the model.

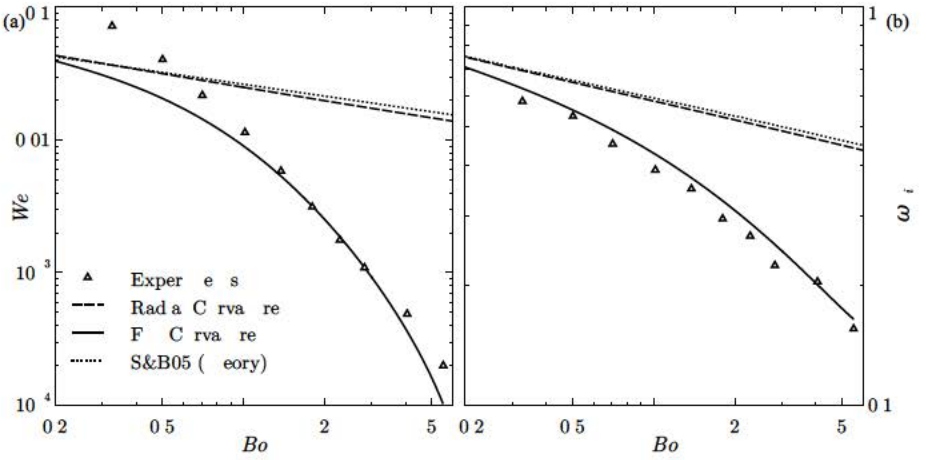

Figure 2.5: Critical Weber number, We_c (a), and critical frequency, $\omega_{c,i}$ (b), as functions of Bo for $\Gamma = 5.83$. The experimental results are plotted with symbols ($\triangle$), solid lines represent the theoretical stability limit given by equation (2.25), and dotted lines are the theoretical results obtained by Sauter & Buggisch (2005), labelled S&B05. The predictions of our model using the slender approximation for the curvature are represented with dashed lines.

These conclusions are not only valid for the particular value of $\Gamma = 5.83$ discussed above, but also apply to arbitrary liquid viscosities, as can be deduced from the analysis of Figure 2.6. The agreement between the predicted and measured values of We_c is especially remarkable for $Bo \gtrsim 1$. The discrepancies observed for the smallest values of Γ and Bo can be attributed to the relaxation experienced by the velocity profile at the exit of the injector, as pointed out by Sevilla (2011). Finally, notice that the validity of the correlation (2.35) is limited to the cases in which the jet is nearly cylindrical, namely for the smallest values of Bo and the largest values of Γ. Specifically, it has been checked that the relative difference

$$\Delta = \frac{|We_c - We_c^{\mathrm{SB}}|}{We_c} \tag{2.36}$$

decreases as the slenderness increases, being $\Delta < 0.1$ only within a small region of the (Bo, Γ) parameter plane, where the conditions $Bo \lesssim 2$ and $\Gamma \gtrsim 400$ are simultaneously accomplished. However, in strongly non-slender cases the relative difference becomes very large, e.g. $\Delta \gtrsim 1000$ for $Bo \gtrsim 5$ and $\Gamma \sim 10$.

The results of Figure 2.6 can also be used to answer the following key question: which is the thinnest steady thread that can be produced at a given

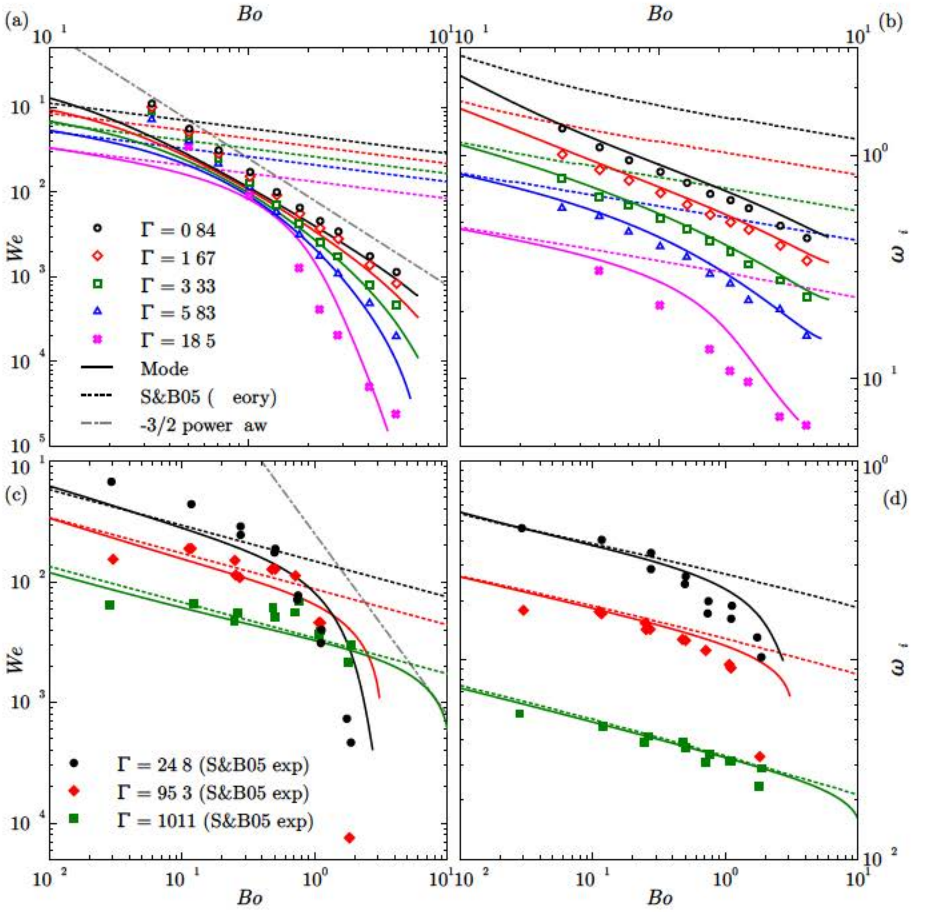

Figure 2.6: Critical Weber number, We_c (left column), and critical frequency, $\omega_{c,i}$ (right column), as functions of Bo for several values of Γ. In the bottom row, three experimental sets extracted from Sauter & Buggisch (2005) have been included. The solid lines represent the predictions of equation (2.25). The dashed lines show the predictions based on the theory of S&B05. The dash-dotted lines in (a) and (c) correspond to $We_c \propto Bo^{-3/2}$ (see the main text for discussion).

distance from the injector thanks to gravitational stretching? Notice first that, for $z \gg 1$, the asymptotic expression for the jet radius is given by

$$r_{j0} \to q^{1/2} (2z)^{-1/4} \tag{2.37}$$

and, therefore,

$$r_{\min} = (2z)^{-1/4} Bo^{3/8} We_c^{1/4}(Bo, \Gamma). \tag{2.38}$$

Equation (2.38) indicates that, for a given Γ, the size of the thread at a fixed axial position decreases when the diameter of the injector increases provided that $We_c \propto Bo^{-n}$ with $n > 3/2$. It can be deduced from Figure 2.6 that the latter condition is fulfilled beyond a certain critical Bond number that depends on Γ. To illustrate this idea, it is interesting to note that, according to equation (2.38) and Figure 2.6, for a liquid with viscosity $\nu = 350$ cSt issuing from a nozzle of radius $R = 3.5$ mm, a steady liquid thread of radius 80 μm can be produced at a distance of 15 cm from the outlet if the amplitude of the external noise is sufficiently small. This type of result would be impossible to predict without the precise theoretical description of the critical flow rate provided here.

2.6 Conclusions and future works

In this chapter, it has been shown that the jetting to dripping transition experienced by highly-stretched free falling vertical liquid jets can be accurately described by the simple one-dimensional mass and momentum equations, provided that the exact expression of the interfacial curvature of the jet is retained in the analysis. It has been demonstrated that axial curvature of the jet, neglected in previous analyses, plays a central role in stabilizing the highly stretched liquid thread. Indeed, the predicted critical flow rates at which the liquid jet is self-excited show a very good agreement with the experimental measurements and are, depending on the Bond and Kapitza numbers, up to three orders of magnitude smaller than those reported in the literature (see e.g. Sauter & Buggisch, 2005). These new results indicate that the size of the micron-sized jets generated at a particular distance from the nozzle outlet can be reduced increasing the exit diameter of millimetric injection tubes.

The linear analysis presented cannot predict the long-time dynamics of globally unstable jets. Indeed, below the critical flow rate, the amplitude of the

self-excited oscillations may either grow in time or evolve towards a limit cycle. In the former case, the jet would disrupt into drops leading to a dripping regime, whereas in the latter, the jet would oscillate without breaking. The analysis of the conditions determining the transition between these two non-linear regimes, which crucially depend on the jet length, is left for a future study.

Finally, it has to be pointed out that the case of strongly stretched jets of low viscosity liquids like water, where $\Gamma \ll 1$, deserves further experimental and theoretical work. Indeed, in the experiments of Clanet & Lasheras (1999), where water was injected through long needles, the viscous relaxation process experienced by the jet downstream of the outlet is known to play an important role in the global stability threshold (Sevilla, 2011). Although relaxation effects cannot be captured with the simple one-dimensional model used in this chapter, the possibility remains that higher-order one-dimensional descriptions that account for radial diffusion, like the parabolic model developed by García & Castellanos (1994), improve the theoretical predictions in cases where viscous relaxation plays an important role, something that should be addressed in a future work. Nevertheless, it is possible that the global mode discovered by Sauter & Buggisch (2005), and revisited in the present work, also could be present in the transition to dripping in highly-stretched jets of low viscosity liquids like water, apart from the self-destabilizing loop described by Umemura & Osaka (2014). To check this hypothesis, new experiments should be performed avoiding viscous relaxation effects, e.g. by means of nozzles or orifices that provide nearly uniform exit velocity profiles.

References

Briggs, R. J. 1964 *Electron-stream interaction with plasmas (Research monograph no. 29)*. MIT Press.

Canuto, C., Hussaini, M. Y., Quarteroni, A. & Zang, T. A. 2006 *Spectral methods. Fundamentals in single domains*. Springer-Verlag.

Clanet, C. & Lasheras, J. C. 1999 Transition from dripping to jetting. *J. Fluid Mech.* 383, 307–326.

Eggers, J. & Dupont, T. F. 1994 Drop formation in a one-dimensional approximation of the navier-stokes equation. *J. Fluid Mech.* 262, 205–222.

Frankel, I. & Weihs, D. 1985 Stability of a capillary jet with linearly increasing axial velocity (with application to shaped charges). *J. Fluid Mech.* 155, 289–307.

García, F. J. & Castellanos, A. 1994 One-dimensional models for slender axisymmetric viscous liquid jets. *Phys. Fluids* 6 (8), 2676–2689.

Guerrero, J., González, H. & García, F. J. 2012 Spatial modes of capillary jets, with application to surface stimulation. *J. Fluid Mech.* 702, 354–377.

Huerre, P. & Monkewitz, P. A. 1985 Absolute and convective instabilities in free shear layers. *J. Fluid Mech.* 159, 151–168.

Keller, J. B., Rubinow, S. I. & Tu, Y. O. 1972 Spatial instability of a jet. *Phys. Fluids* 16, 2052–2055.

Landau, L.D. 1946 On the vibrations of the electronic plasma. *J. Phys. U.S.S.R.* 10 (25), 445–460.

Le Dizès, S. 1997 Global modes in falling capillary jets. *Eur. J. Mech. B/Fluids* 16, 761–778.

Leib, S. J. & Goldstein, M. E. 1986 The generation of capillary instabilities on a liquid jet. *J. Fluid Mech.* 168, 479–500.

Plateau, J. 1873 *Statique Expérimentale et Théorique des Liquides*. Gauthier-Villars et C^{ie}, Paris.

Rayleigh, W. S. 1878 On the instability of jets. *Proc. London Math. Soc.* 10, 4–13.

Sauter, U. S. & Buggisch, H. W. 2005 Stability of initially slow viscous jets driven by gravity. *J. Fluid Mech.* 533, 237–257.

Schulkes, R. M. S. M. 1994 The evolution and bifurcation of a pendant drop. *J. Fluid Mech.* 278, 83–100.

Senchenko, S. & Bohr, T. 2005 Shape and stability of a viscous thread. *Phys. Rev. E* 71, 056301.

Sevilla, A. 2011 The effect of viscous relaxation on the spatiotemporal stability of capillary jets. *J. Fluid Mech.* 684, 204–226.

Tomotika, S. 1936 Breaking up of a drop of viscous liquid immersed in another viscous fluid which is extending at a uniform rate. *Proc. Roy. Soc.* 153, 302–318.

Umemura, A. & Osaka, J. 2014 Self-destabilizing loop observed in a jetting-to-dripping transition. *J. Fluid Mech.* 752, 184.

CHAPTER
THREE

Dripping dynamics at high Bond numbers

Contents

3.1 Introduction

Once seen in Chapter 2 the important role of the injector size in the jetting to dripping transition, it is natural to revisit the problem of drop formation, the rich dynamics present in the dripping regimes and the transition to jetting when varying the size of the outlet. As mentioned in Chapter 1, drop formation is a phenomenon present in nature, everyday life situations, industrial processes and science applications.

The dynamics before and after pinch-off was studied in the inviscid case in the pioneering experimental work of Peregrine *et al.* (1990), using a liquid bridge as a model system, as will be done in the next chapter of the present Thesis. Shi *et al.* (1994) extended the work of Peregrine *et al.* (1990) to higher viscosities and both Zhang & Basaran (1995) and Brenner *et al.* (1997) provided time-resolved images of the bifurcations of a pendant drop.

In the inviscid limit, drop formation was studied numerically by Schulkes (1994) using an axisymmetric boundary integral method. Taking advantage of the development of the one-dimensional (1D) equations, the first attempts to simulate the formation of viscous drops at a very reduced computational cost dealt with the quasi-steady growth of the droplet (Eggers & Dupont, 1994; Brenner *et al.*, 1997). The drop formation process at a nonzero Weber number was thoroughly studied in the works of Prof. Basaran's group, both from the numerical and the experimental points of view, e.g. in the work of Wilkes *et al.* (1999) where the phenomenon is explored for wide ranges of the governing parameters. Later on, to show the capabilities and limitations of the 1D model, Ambravaneswaran *et al.* (2002) compared their results with 2D simulations of the Navier-Stokes equations, finding that the agreement between both models is remarkable specially when surface tension forces dominate the problem.

The effect of viscosity in the transition from dripping to jetting, not on the reverse transition, was studied in Ambravaneswaran *et al.* (2004) by numerically simulating the 1D equations. Their numerical work revealed that, when the liquid viscosity is large enough, the dripping to jetting transition takes place in the absence of the intermediate chaotic dripping regimes observed in the case of low viscosity liquids (Clanet & Lasheras, 1999; Coullet *et al.*, 2005). In addition, and making use of simple scaling arguments, Ambravaneswaran *et al.* (2004) derived criteria to predict the transition to jetting. In a more extensive work, accompanied by experiments, Subramani *et al.* (2006) characterized the dripping regimes through bifurcations and phase diagrams, showing the high complexity of the phenomena when varying the governing parameters. However, these valuable works were performed at small Bond numbers, $Bo \leq 0.5$, far below the values studied in the present chapter.

For small enough flow rates, main droplets as well as tiny satellite drops are formed periodically. As the flow rate is increased, satellites are no longer present, giving way to a period-1 dripping regime without satellite droplets (Zhang & Basaran, 1995; Zhang, 1999; Ambravaneswaran *et al.*, 2002). If the flow rate is further raised, the transition to jetting takes place. Depending on the liquid viscosity, this transition can be preceded by more complex regimes, namely period-2, period-4, chaotic dripping etc. as mentioned above.

The purpose of this chapter is to extend the works of Ambravaneswaran *et al.* (2004) and Subramani *et al.* (2006) to higher Bond numbers by performing new experiments, describing the effect that the increase of the injector size has on the fascinating non-linear dynamics present in a leaky faucet, as well as on the

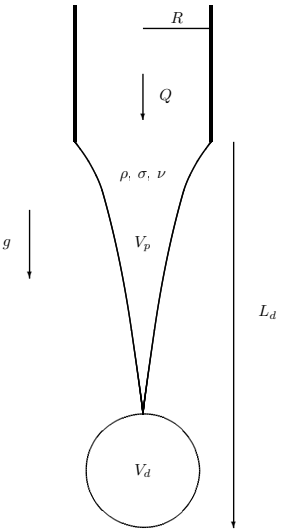

Figure 3.1: Sketch of the flow configuration and variables used for the analysis of the experiments.

jetting transition.

3.2 Problem description

To characterize the dynamics of the dripping regimes as well as the jetting transition, the same parameters as in Ambravaneswaran *et al.* (2004) have been used. Consider a Newtonian liquid of constant and uniform properties, namely density ρ, kinematic viscosity ν and surface tension coefficient σ issuing from a capillary tube of radius R, at a constant flow rate Q. In presence of gravity g, and in a quiescent surrounding atmosphere, the drops growing and detaching from the outlet can be characterized by the volume of the detached drop V_d, the volume of the liquid that remains pending attached to the outlet V_p, and the limiting length L_d, defined as the distance from the tube at the moment of the break-up. A sketch of the flow and the definition of the relevant variables can be observed in Figure 3.1.

The experimental setup was the same as the one used to study the jetting to dripping transition, described in Section 2.5, and therefore similar to those used in previous studies of jet and drop formation (Wilkes *et al.*, 1999; Subramani *et al.*, 2006). The properties of the different liquids used in the present chapter can be found in Table 3.1.

ν [mm^2 s^{-1}]	ρ [kg m^{-3}]	σ [mN m^{-1}]	Γ
2	833	18.3	3.31×10^{-2}
5	915	19.7	8.40×10^{-2}
10	935	20.1	1.68×10^{-1}
20	950	20.6	3.34×10^{-1}
50	960	20.8	8.36×10^{-1}

Table 3.1: Properties at 25 °C of the Sigma-Aldrich silicon oils used in the present chapter. The last column represents the Kapitza number, $\Gamma = 3\nu(\rho^3 g/\sigma^3)^{1/4}$, computed using a value of $g = 9.81$ ms^{-2}.

The governing parameters of the experiments are the liquid properties ρ, ν and σ, the injector size R and the injection flow rate Q. Non-dimensionally, the dripping and jetting dynamics can be described through the values of three parameters, namely the Bond, $Bo = \rho g R^2/\sigma$, Weber, $We = \rho U^2 R/\sigma$, and Kapitza, $\Gamma = 3\nu(\rho^3 g/\sigma^3)^{1/4}$, numbers defined as in Chapter 2, with $U = Q/(\pi R^2)$. Traditionally, the Ohnesorge number $Oh = \eta/\sqrt{\rho R \sigma}$, being $\eta = \rho\nu$ the dynamic viscosity of the liquid, has been used in these type of studies. Nevertheless, the use of Γ results a more natural choice, because its value depends only on the liquid properties for a given value of g. Thus, a change in the value of Γ implies only a variation of the working fluid. In contrast, when using Oh as a governing parameter, its change can be associated either with a variation of the liquid properties or a change in the injector size.

3.3 Results

The rich non-linear dynamics of the dripping regime can be appreciated by observing the wide diversity of responses present in a dripping faucet when varying the governing parameters. The results presented in Figure 3.2(a) show an example of periodic dripping, in which all the main drops detached from the tube are equal in size and the pinch-off occurs at the same point. This fact means that there is a single value of both L_d/R and of V_d/V_p for a given value of the Weber number. This regime is known in the literature as period-1 or P1, and constitutes the simplest possible dripping behaviour. In contrast, if the drops alternatively detach at two different lengths from the outlet, with two different shapes respectively, the regime is known as period-2, or P2. There

are also examples of odd-dynamics, such as period-3 regime or P3, reported in the literature. In addition, apart from these periodic regimes, the ejected drops may exhibit a chaotic behaviour, CD, with different volumes and detachment lengths without following any repeatable pattern.

The periodic regimes P1, P2 and P3 described in the previous paragraph are depicted in Figures 3.2(a), (b) and (c) respectively. Figure 3.3(a) shows an example of chaotic dripping while in Figure 3.3(b) the values of the dimensionless detachment length for i consecutive droplets are represented, confirming the chaotic behaviour of the regime. The values of the governing parameters in each case can be found in the corresponding figure captions.

It is important to point out that the presence of satellite droplets will be addressed in Section 3.3.3. Therefore, in the dripping regimes mentioned above, and summarized in the phase maps presented in the following sections, there is not an explicit differentiation between cases with and without satellites, provided that the main droplets exhibit the same behaviour.

3.3.1 Dripping to jetting transition. Phase diagrams at constant Kapitza number

There are many examples in the literature in which qualitative or ad-hoc criteria are used to decide when the transition to jetting takes place. As an example, Clanet & Lasheras (1999) considered that the jetting regime occurred when the value of the limiting length accomplished the criterion $L_d/R \sim 20$. Nevertheless, this approach, which is valid in the case of water in a first approximation, fails when the viscosity of the liquid increases. Therefore, the criterion used in the present work follows that of Ambravaneswaran *et al.* (2004): the transition to jetting can be easily identified because values of L_d/R and V_d/V_p undergo sudden and large changes at the same time, as clearly evidenced in Figure 3.4. The detachment length increases abruptly at a value of $We = We_j$, as can be appreciated in Figure 3.4(a), while the volume ratio suddenly decreases at the same Weber number We_j, as represented in Figure 3.4(b). In addition, the shaded region represents the hysteresis associated with both transitions (Clanet & Lasheras, 1999). Once a jet is formed, the flow rate can be reduced below the value of We_j prior to drop formation. Thus, the jetting to dripping transition occurs at a Weber number $We_d < We_j$.

The same analysis has been performed for different values of Bo, as summarized in Figure 3.5. The shadowed zones in Figure 3.5 correspond again to

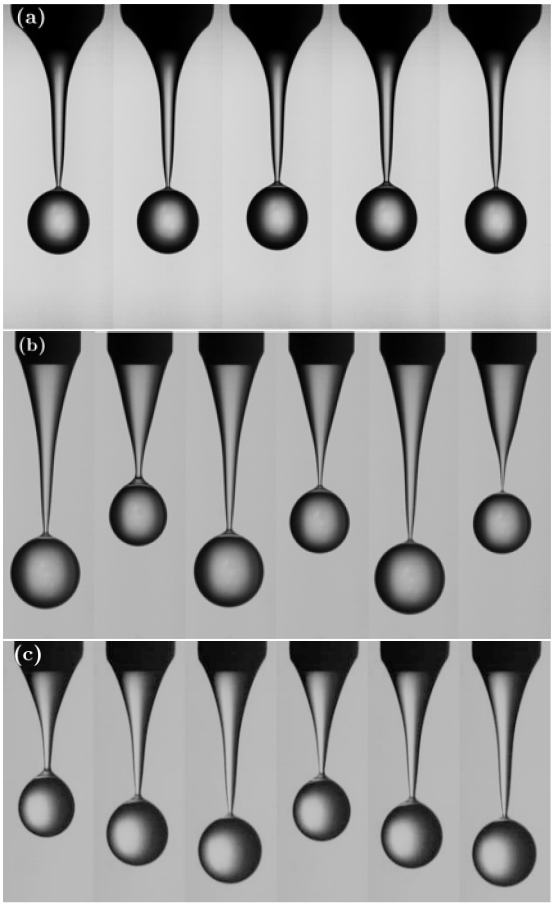

Figure 3.2: Examples of consecutive drops in the case of P1 regime (a), P2 (b) and P3 (c). The values of the governing parameters in each case are $Bo = 2.2$, $We = 1.11 \times 10^{-2}$, $\Gamma = 0.17$ (a), $Bo = 0.7$, $We = 6.65 \times 10^{-2}$, $\Gamma = 0.33$ (b) and $Bo = 1.0$, $We = 4.69 \times 10^{-2}$, $\Gamma = 0.17$ (c).

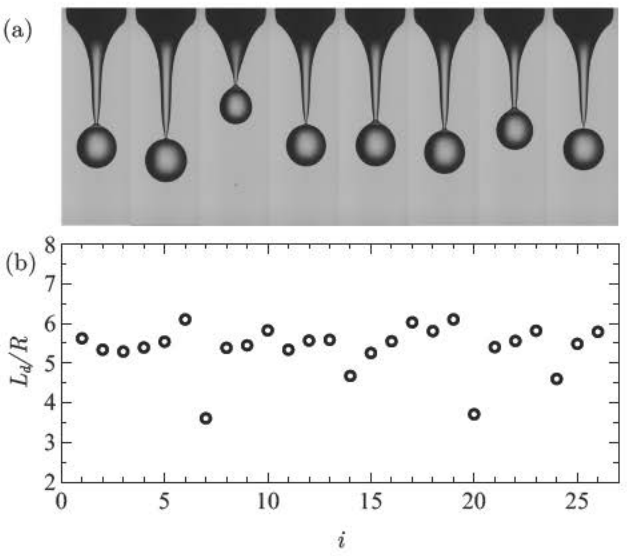

Figure 3.3: Consecutive drops in the chaotic dripping regime (a) and values of the dimensionless limiting length (b) for $Bo = 2.2$, $We = 1.46 \times 10^{-2}$, $\Gamma = 0.084$.

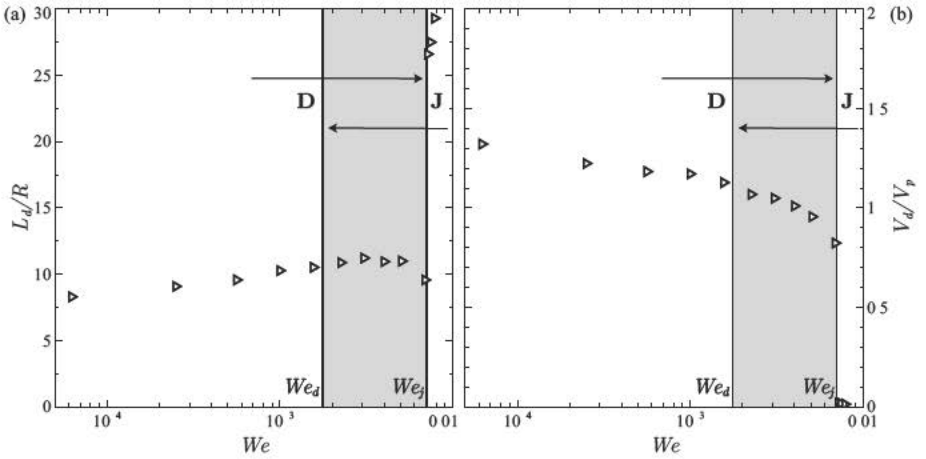

Figure 3.4: Non-dimensional limiting length L_d/R (a) and detached to pendant volume ratio V_d/V_p (b) as functions of Weber number We, for $Bo = 3.42$ and $\Gamma = 0.84$. The vertical lines represent the critical values of Weber number at which the transition to jetting takes place We_j, and the jetting to dripping transition We_d. Hysteresis exists in the shaded region.

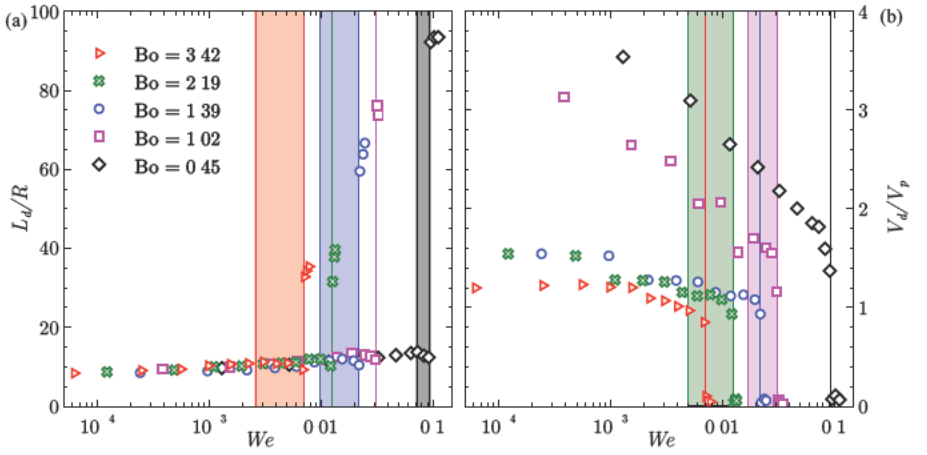

Figure 3.5: Dimensionless limiting length L_d/R (a) and volume ratio V_d/V_p (b) as functions of Weber number We, for $\Gamma = 0.84$ and several values of Bo. The vertical lines represent the transition to jetting, and the shadowed zones correspond to the hysteresis associated with both transitions.

the hysteresis of the transition for each value of Bo, and have been plotted alternatively in Figures 3.5(a) and (b), to avoid the overlapping of the hysteretic regimes, and thus to ease the reading of the plots. As observed by Clanet & Lasheras (1999) in the case of water, it is clear that the hysteresis increases with the Bond number. It should be highlighted that this hysteresis had not been previously quantified for any liquid different from water.

Figure 3.6(a) shows the experimental value of We_j as a function of Bo for a given liquid, that is, for a fixed value of Γ. This boundary, represented by the symbols $\triangle$, divides the Bo-We plane into two regions, yielding a phase map in which points above the curve correspond to a jetting regime, labelled J in the figures. Below this critical curve, in the zone labelled P1, the behaviour corresponds to period-1 regime. Thus, this is an example of simple dynamics, as defined in Subramani *et al.* (2006), being the possible responses either P1 or J.

The hysteresis present in the transition can also be observed in Figure 3.6(a) for $\Gamma = 0.84$ corresponding to the silicone oil of kinematic viscosity $\nu = 50$ cSt, where the symbols ∇ represent the boundary for the jetting to dripping transition. The shadowed zone corresponds to points of the Bo-We parameter plane where the regime is P1 when increasing the flow rate. However, if the jet is previously formed, and then the value of We is decreased, the corresponding

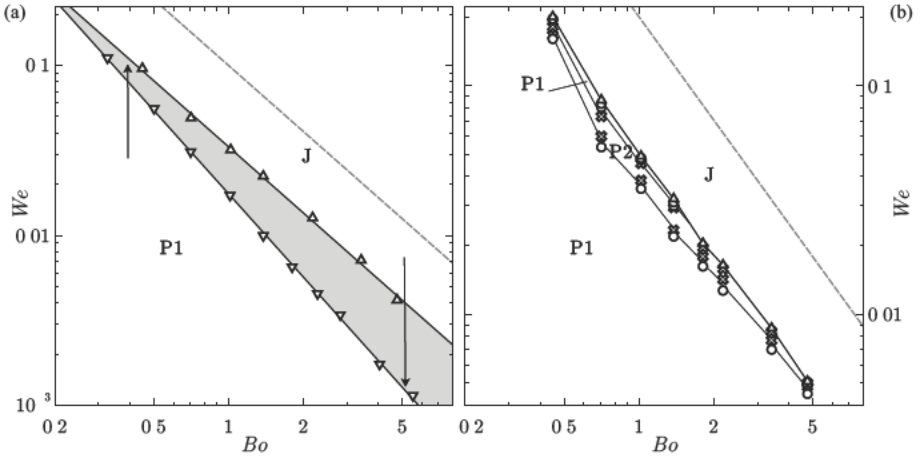

Figure 3.6: Phase maps showing the regimes in the (Bo, We) parameter plane when $\Gamma = 0.84$ (a) and $\Gamma = 0.33$ (b). The symbols represent the experimental transition points. The regions are labelled P1 for period-1 dripping, P2 for period-2 dripping and J for jetting. In Figure (a) the shaded area corresponds to the hysteresis of the dripping to jetting transition, marked with the symbol $\triangledown$. The dashed line shows the fitted power law $We_j \sim Bo^{-n}$, with $n = 1.3$ (a) and $n = 1.5$ (b).

regime is jetting inside the shaded area.

Figure 3.6(b) represents another phase map in the Bo-We plane for a different value of $\Gamma = 0.33$, corresponding to a liquid of kinematic viscosity $\nu = 20$ cSt. The responses present here are referred to as 'complex dynamics' in Subramani *et al.* (2006). Indeed, there exists another regime besides the P1 and J behaviours. Specifically Figure 3.6(b) reveals that there is a region delimited by crosses in which the observed regime is P2. In agreement with the results of Ambravaneswaran *et al.* (2004), the P2 zone is found when increasing the Weber number right after P1. It is also worth pointing out that there is a narrow P1 zone before the transition to jetting for small Bond numbers, as reported in Subramani *et al.* (2006) for a value of $Bo = 0.3$.

Making use of simple scaling arguments Ambravaneswaran *et al.* (2004) provided criteria to predict the dripping to jetting transition, by comparing the timescales present in the problem. In particular, they argued that the critical Weber number We_j varies with the Ohnesorge number, being $We_j \sim \mathcal{O}(1)$ for $Oh \ll 1$; $We_j \sim Oh^{-6}$ for $Oh \sim 1$ and $We_j \sim Oh^{-2}$ for $Oh \gg 1$. Nevertheless, these scalings, which are in agreement with the simulations presented in Ambravaneswaran *et al.* (2004) and Subramani *et al.* (2006), at

small Bond numbers, are unable to capture the experimental results presented here for larger values of Bo. The experimental results shown in Figure 3.6 can be fitted to a power law $We_j \sim Bo^{-n}$, obtaining $n \approx 1.3$ in the case of $\Gamma = 0.83$, and $n \approx 1.5$ when $\Gamma = 0.33$. These power laws are represented with dashed lines in Figure 3.6. This strong dependence on the Bond number for a fixed value of Γ suggests that the scaling laws preiously proposed in the literature must be reconsidered. In fact, making use of the relationship $\Gamma = 3OhBo^{1/4}$, the prediction $We_j \sim Bo^{-3/2}$ for the silicon oil of $\nu = 20$ cSt yields $We_j \sim Oh^6$ which is in marked contradiction with the scaling law proposed in Ambravaneswaran *et al.* (2004) for intermediate Ohnesorge numbers, namely $We_j \sim Oh^{-6}$.

3.3.2 Phase diagrams at constant Bond number

To illustrate the effect of the viscosity on the dynamics the results have also been represented in a Γ-We plane at a constant value of Bo. Figure 3.7(a) shows the results for the case $Bo = 1.0$, while in $Bo = 2.2$ in Figure 3.7(b). In agreement with the results of Ambravaneswaran *et al.* (2004) and Subramani *et al.* (2006), it can be observed that the decrease of the viscosity of the liquid leads to more complex dynamics. Thus, a region of chaotic dripping at small values of Γ can be found in Figure 3.7. In addition, it is clear from Figure 3.7 that there exists a critical value of Γ_c which divides the phase diagrams into two zones, one with simple dynamics for $\Gamma > \Gamma_c$ and other for $\Gamma < \Gamma_c$ where regimes other than P1 and J can be found. It is because of this reason that the viscosities of the liquids used for the experiments reported in this chapter are smaller than those considered in Chapter 2. Note that larger values of Γ lead to phase maps qualitatively similar to that already discussed in Figure 3.6(a).

The choice of $Bo = 1.0$ allows a comparison with the numerical results of Subramani *et al.* (2006). In their work, the authors present only a few computations to illustrate the dynamics at high Bond numbers. It should be highlighted that the value of $Bo \approx 0.96$ considered by Subramani *et al.* (2006) although high compared with the values $Bo \approx 0.3$ and $Bo \approx 0.5$ thoroughly studied in previous works is still much smaller than the value $Bo \approx 5$ reached in the present study. Figure 3.7(a) shows a small region of odd-dynamics, namely period-3, in fair agreement with the values $Bo = 0.97$, $We = 0.05$, $\Gamma = 0.3$ reported by Subramani *et al.* (2006).

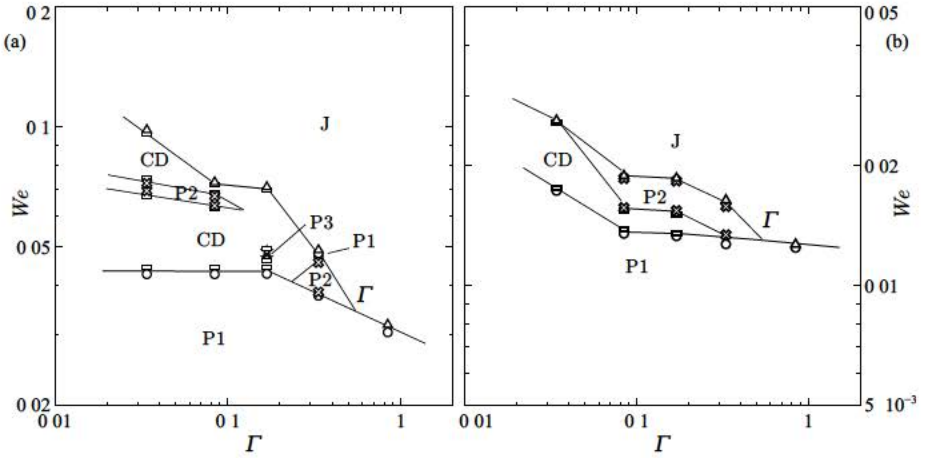

Figure 3.7: Phase maps showing the regimes present in the (Γ, We) parameter plane for $Bo = 1.0$ (a) and $Bo = 2.2$ (b). The symbols represent the experimental transition points. The regions are labelled P1 for period-1, P2 for period-2 and P3 for period-3 dripping. CD stands for chaotic dripping, and J for jetting.

3.3.3 Satellite drops

The analysis of the experiments performed in the present work allows also to distinguish the cases in which there exist satellites between the main drops. The occurrence of satellite drops has been previously analysed with different approaches. Using the VOF numerical method, Zhang (1999) derived a correlation for the limiting Weber number for satellites to exist, namely

$$WeBo^{0.3921} = K, \tag{3.1}$$

with $K = 0.0125$. However, this correlation does not take into account the effect of liquid properties, due to the failure of the code by Zhang (1999) to converge at moderate to high values of the Ohnesorge numbers. In Ambravaneswaran *et al.* (2002), the authors performed 1D computations to depict the boundary of satellite formation when varying the value of Oh but, again, only for $Bo = 0.3$.

In a study of the viscous Savart sheet, Villermaux *et al.* (2013) performed dripping experiments at high Bond numbers to explain the bimodality of the droplet size distribution. In particular, by comparing the concomitant effects of viscosity, capillary destabilization and the recoiling of the filament that appears after pinch-off, the authors provide an explanation both for the presence of one small satellite droplet per main drop, and for the ratio of the satellite to main

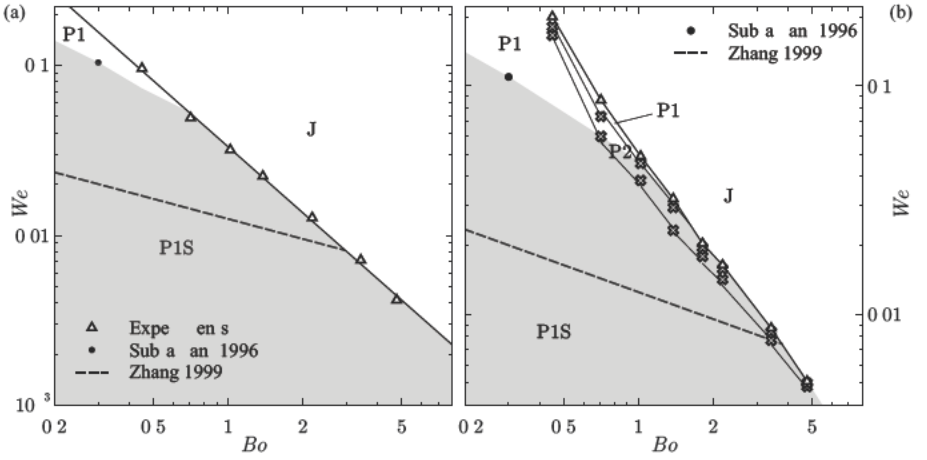

Figure 3.8: Existence of satellite drops in the (Bo, We) parameter plane (shaded areas) for $\Gamma = 0.84$ (a) and $\Gamma = 0.33$ (b). The results of Subramani *et al.* (2006) have been included with filled symbols, and the dashed line represents the correlation numerically derived by Zhang (1999).

drop size. However, the liquid used in their experiments corresponds to a value of $\Gamma = 2.19 > \Gamma_c$ and thus observing only simple dynamics. In their model experiment they used a value of $Bo = 2.15$ which is in agreement with the results presented above.

Figure 3.8 shows the regions where satellite drops are present in the We-Bo plane for two different values of Γ. The shadowed areas correspond to satellite formation, and the dashed line is the correlation derived by Zhang (1999) through numerical simulations. The points from Ambravaneswaran *et al.* (2002) and Subramani *et al.* (2006) are also included in the figure for completeness.

It is clear from Figure 3.8 that the increase of the injector radius leads to the presence of satellite droplets in regions different from P1. As an example, Figure 3.9 shows a new variation of the P2 regime that was never reported before. While Figure 3.2(b) depicts the period-2 regime known up to date, namely, without satellite droplets, the experiments performed in the present work reveal that if the Bond number is high enough, satellite droplets detach after the drop that pinches off further from the outlet. This new regime, called P2S1, can be observed in Figure 3.9(a). Moreover, for still higher values of Bo, there exists another regime with satellites after each detachment of a main drop, both the first one, further from the injector, and the second one, closer to the outlet, referred to as P2S2 regime. This regime is illustrated in Figure 3.9(b). It

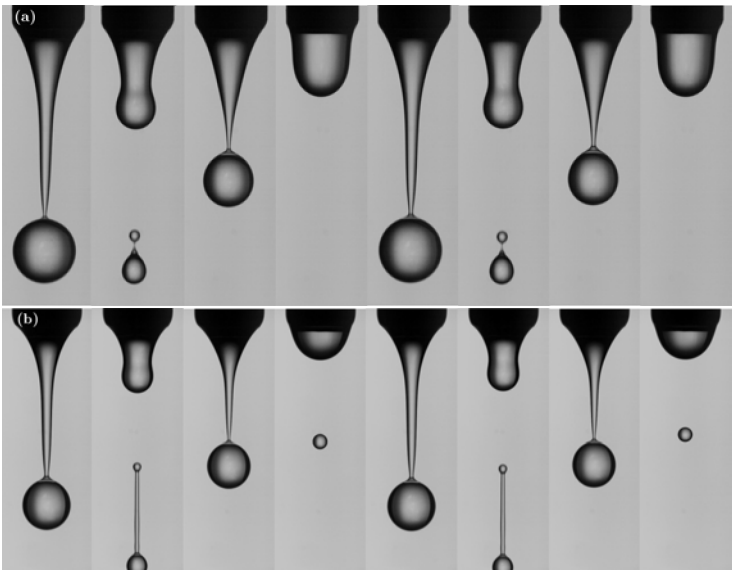

Figure 3.9: Example of satellites presence in period-2 regime, showing the case of P2S1 for $Bo = 1.38$, $We = 2.93 \times 10^{-2}$ and $\Gamma = 0.17$ (a) and P2S2 for $Bo = 2.2$, $We = 1.53 \times 10^{-2}$ and $\Gamma = 0.17$.

should be pointed out that the presence of satellite droplets in period-2 dripping has not been previously reported, since large enough injector sizes are needed for their appearance, and all the previous studies were done for values of the Bond number too small for the existence of these new regimes.

3.4 Conclusions and future works

In this chapter, both the dripping dynamics and the transition to jetting have been revisited through new experiments, reaching values of Bo up to one order of magnitude larger than in previous studies on drop formation. As suggested by Subramani *et al.* (2006), it has indeed been shown in the present chapter that larger injector sizes increase the complexity exhibited by a leaky faucet, to such an extent that the previous scaling laws (Ambravaneswaran *et al.*, 2004) break down when the value of Bo varies in a wide range. The comprehensive experimental work has been summarized through new phase diagrams, based on the dimensionless parameters more adequate than those used in the previous studies, using the Kapitza number Γ, which depends only on the liquid properties, instead of the Ohnesorge number Oh. In addition, and thanks to

the experimental results of Chapter 2, the hysteresis of the dripping to jetting transition has been quantified for the first time for a working liquid different from water, namely $\nu = 50$ cSt. Finally, new regimes with satellite droplet formation have been found at high enough values of Bo.

The phase maps depicted in this chapter could be improved by adding points in the regions where the dynamics results more interesting. This could be done either by means of numerical simulations or by performing new experiments, with the purpose of overcoming the limitations associated with the discrete experimental points reported in this study: smooth variations in the parameter space through experiments imply the need of an even more intensive experimental sweep than those already performed in this chapter. Moreover, it would be interesting to extend the quantification of the hysteresis to other viscosities apart from the one presented here. In addition, the influence of the injector radius on the transition to jetting clearly deserves further theoretical effort, aimed at deriving new scaling laws able to account for this effect.

References

Ambravaneswaran, B., Subramani, H. J., Phillips, S. D. & Basaran, O. A. 2004 Dripping-jetting transitions in a dripping faucet. *Phys. Rev. Lett.* 93, 034501.

Ambravaneswaran, B., Wilkes, E. D. & Basaran, O. A. 2002 Drop formation from a capillary tube: Comparison of one-dimensional and two-dimensional analyses and occurrence of satellite drops. *Phys. Fluids* 14, 2606–2621.

Brenner, M. P., Eggers, J., Joseph, K., Nagel, S. R. & Shi, X. D. 1997 Breakdown of scaling in high Reynolds number droplet fission. *Phys. Fluids* 9, 1573–1590.

Clanet, C. & Lasheras, J. C. 1999 Transition from dripping to jetting. *J. Fluid Mech.* 383, 307–326.

Coullet, P., Mahadevan, L. & Riera, C. S. 2005 Hydrodynamical models for the chaotic dripping faucet. *J. Fluid Mech.* 526, 1–17.

Eggers, J. & Dupont, T. F. 1994 Drop formation in a one-dimensional approximation of the navier-stokes equation. *J. Fluid Mech.* 262, 205–222.

Peregrine, D. H., Shoker, G. & Symon, A. 1990 The bifurcation of liquid bridges. *J. Fluid Mech.* 212, 25.

Schulkes, R. M. S. M. 1994 The evolution and bifurcation of a pendant drop. *J. Fluid Mech.* 278, 83–100.

Shi, X. D., Brenner, M. P. & Nagel, S. R. 1994 A cascade of structure in a drop falling from a faucet. *Science* 265, 219–222.

Subramani, H. J., Yeoh, H. K., Suryo, R., Xum, Q., Ambravaneswaran, B. & Basaran, O. A. 2006 Simplicity and complexity in a dripping faucet. *Phys. Fluids* 18, 032106.

Villermaux, E., Pistre, V. & Lhuissier, H. 2013 The viscous Savart sheet. *J. Fluid Mech.* 730, 607–625.

Wilkes, E. D., Phillips, S. D. & Basaran, O. A. 1999 Computational and experimental analysis of dynamics of drop formation. *Phys. Fluids* 11, 3577–3598.

Zhang, X. 1999 Dynamics of growth and breakup of viscous pendant drops into air. *J. Colloid Sci.* 212, 107.

Zhang, X. & Basaran, O. A. 1995 An experimental study of dynamics of drop formation. *Phys. Fluids* 7, 1184.

CHAPTER
FOUR

Thinning of particulate suspensions near pinch-off

Contents

4.1 Introduction

As pointed out in Chapter 1, colloidal suspensions are present in a number of applications, and the basic knowledge about the detailed dynamics of drop and jet formation with these kind of complex fluids is, at least, a step behind their Newtonian counterpart.

After the pioneering work of Nicolas (2002) on gravity-driven suspension jets, the first authors to identify different stages in the pinch-off of a suspension were Furbank & Morris (2004, 2007). They defined an early stage in which the suspension behaves like a continuum medium, characterized by an effective viscosity. While the presence of particles increases this viscosity, experimental measurements suggest that in the second regime the thinning of the ligament

no longer follows the behaviour predicted by the effective viscosity, being accelerated due to effects associated with finite particle size. Precisely this second regime was thoroughly studied by Lidner and coworkers (Bonnoit *et al.*, 2012; Brertrand *et al.*, 2012; Van Deen *et al.*, 2013) with a large set of dripping experiments of polystyrene beads in silicone oil, varying the concentration and the particle size. Specifically, they looked at the evolution of the minimum diameter, and compared it with several Newtonian oils of different viscosities, establishing that the presence of particles accelerates the break-up. More recent and thorough experiments due to Mathues *et al.* (2015) revealed that the neck thinning process decelerates again during the final stages prior to break-up and approaches the behaviour of the matrix fluid close to the pinch-off event. Until recently (Lidner *et al.*, 2015; Zhao *et al.*, 2015), this deceleration stage had not been detected in experimental studies.

The accelerated thinning mentioned above arises from variations in local particle density. As the filament becomes thinner, these variations are amplified, leading ultimately to sections of the filament containing no particles. Sections of the filament with a low particle density have a lower effective viscosity and therefore the thinning dynamics is accelerated. To test this hypothesis, McIlroy & Harlen (2014) made use of a simple one-dimensional model in which the viscosity is determined from the local particle density, found by tracking individual particles within the suspension. In the latter model, particles only contribute to the dynamics through the local viscosity, so the direct effects of hydrodynamic interactions and effects of the individual particles on the free surface are not included. Nonetheless, their model is able to reproduce the accelerated thinning found in the experiments, as shown by Mathues *et al.* (2015), where the self-similar Newtonian scalings are used to support the hypothesis of a solvent-governed break-up. Nevertheless, the final self-accelerated stage is not properly described by the numerical simulations of McIlroy & Harlen (2014) in the important case of small particles and high concentrations, and therefore deserves further analysis. Actually, the hypothesis of a Newtonian break-up governed by the solvent properties proposed by Mathues *et al.* (2015) is motivated by the fact that in the decelerated zone both the fitted viscosity from the experimental thinning data and the rescaled profiles coincide with the liquid properties. However, the number of experimental points gathered during this stage is quite limited, so additional evidence is needed.

The purpose in this chapter is to model the final thinning stages of the liquid trapped between two particles of finite diameter as a stretching Newtonian

liquid bridge with a non-uniform prescribed movement of the confining particles. The starting point of the present modelling effort is the work of McIlroy & Harlen (2014), which shows why initially randomly distributed particles lead to local viscosity variations that amplify into regions of accelerated thinning and eventually lead to particle-free filaments. Precisely this late stage, which seems to be solvent-governed is modelled here numerically, thereby complementing the work by Mathues *et al.* (2015).

4.2 Problem definition

4.2.1 Physical description

Capillary break-up experiments were performed with a CaBER-1 extensional rheometer from Thermo Scientific. Sample volumes of the suspensions were loaded between two circular disks, which were later separated to create an unstable liquid bridge. The evolution of the filament was monitored with a high-speed camera, equipped with a lens system that provides resolution enough to identify individual particles in the suspension filament. More details of the experimental procedure can be found in Mathues *et al.* (2015), and the setup is thoroughly described in Mathues (2015).

Once the suspension sample is stretched, it follows the evolution qualitatively described in Section 4.1. When the concentration fluctuations lead to a particle-free section in the filament, the interstitial fluid thins until the break-up occurs between two end particles, which can be clearly identified as in Figure 4.1. This process resembles the small-scale stretching of a Newtonian filament, in which the particles play the role of moving end-plates. Thanks to the spatial resolution of the experiments, the particles can be tracked over time, providing the stretching velocity profile of the fictitious boundaries associated with the continuous phase thinning.

The suspensions used consisted of non-Brownian spherical particles, dispersed in polydimethylsiloxane oils, whose properties are summarized in Table 4.1. As a reference case, a suspension of volume fraction $\phi = 10\%$ of polystyrene particles with radius $R_p = 20$ μm, 10PS20, diluted in a PDMS oil of viscosity $\eta = 360$ mPa s, shall be considered. Other systems are also studied in the present chapter, varying the particle size, the concentration, and the matrix viscosity. All the experimental input in this chapter has been provided by Wouter Mathues and Christian Clasen, from KU Leuven.

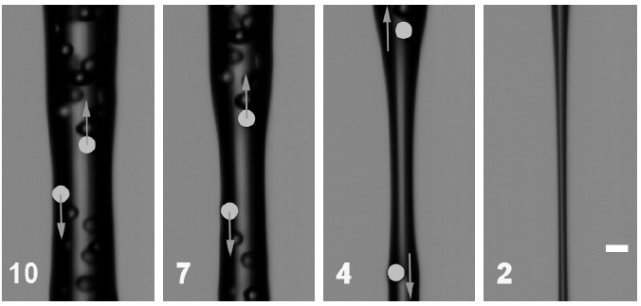

Figure 4.1: Magnified images of the final stages of the capillary break-up of 10% PS20 in PDMS2. The number in the bottom left corner indicates the time to pinch-off $\bar{t}_p - \bar{t}$ in ms and the scale bar represents 50 μm. The final thinning takes place between two particles which are highlighted by the grey circles. Figure taken from Mathues *et al.* (2015).

	η [mPa s]	ρ [kg m^{-3}]	σ [mN m^{-1}]
PDMS 1	180	1070	21.0
PDMS 2	360	970	21.0

Table 4.1: Properties at 25 °C of the Sigma-Aldrich silicone oils used as suspension matrices.

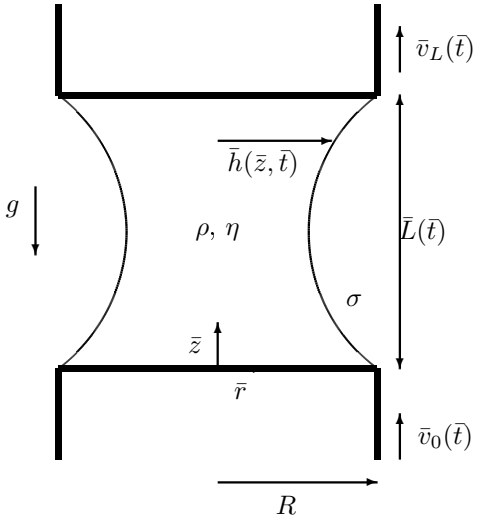

Figure 4.2: Sketch of the flow configuration and the variables used in the model.

4.2.2 Mathematical model

To describe the temporal evolution of the small-scale stretching filament, the fluid trapped between the two end particles is modelled as a Newtonian liquid bridge. Therefore, a liquid of constant density ρ, surface tension coefficient σ, and dynamic viscosity η is considered, corresponding to the fluid used as the suspending medium. The liquid is held captive between two circular plates of radius R, which move vertically with velocities $\bar{v}_0\left(\bar{t}\right)$ and $\bar{v}_L\left(\bar{t}\right)$, in presence of the gravitational field g. Thus, the distance between the plates $\bar{L}\left(\bar{t}\right)$ is a function of time. A sketch of the flow configuration can be observed in Figure 4.2.

Considering the liquid bridge axisymmetric, and neglecting the effect of the surrounding atmosphere, the local radius $\bar{h}\left(\bar{z},\bar{t}\right)$ and axial velocity $\bar{u}\left(\bar{z},\bar{t}\right)$ can be modelled using the one dimensional equations for mass and momentum conservation, derived by Eggers & Dupont (1994),

$$\frac{\partial h^2}{\partial t}+\frac{\partial (h^2 u)}{\partial z}=0, \tag{4.1}$$

$$\frac{1}{Oh^2}\left(\frac{\partial u}{\partial t}+u\frac{\partial u}{\partial z}\right)=-\frac{\partial \mathcal{C}}{\partial z}+\frac{3}{h^2}\frac{\partial}{\partial z}\left(h^2\frac{\partial u}{\partial z}\right)-Bo\left(1+\frac{a_0}{g}\right), \tag{4.2}$$

where the curvature $\mathcal{C}$ in the pressure gradient term is given by

$$\mathcal{C} = h^{-1}\left[1+\left(\frac{\partial h}{\partial z}\right)^2\right]^{-1/2} - \frac{\partial^2 h}{\partial z^2}\left[1+\left(\frac{\partial h}{\partial z}\right)^2\right]^{-3/2}, \tag{4.3}$$

retaining its full expression that includes both the radial and the axial terms.

The variables in (4.1)-(4.3) have been made dimensionless using the plate radius as characteristic lengthscale, $z_c = R$, and the viscous-capillary velocity $u_c = \sigma/\eta$ as the velocity scale. Thus, the system (4.1)-(4.2) only depends on the Ohnesorge number, $Oh = \eta/\sqrt{\rho\sigma R}$, the Bond number $Bo = \rho g R^2/\sigma$, and the non-dimensional inertia a_0/g, being $a_0 = \mathrm{d}\bar{v}_0/\mathrm{d}\bar{t}$, which must be taken into account because of the election of the accelerating Eulerian frame moving with the lower end-plate. Notice that throughout this chapter, barred symbols denote dimensional variables.

The contact line is assumed to be pinned to the plates, $h(0,t) = h(L,t) = 1$, and in the moving frame of reference considered, the bottom plate is steady $u(0,t) = 0$, while the upper one moves with velocity $u(L,t) = v = v_L(t) - v_0(t)$.

As initial condition for the temporal evolution, the simplest choice would consider the bridge as a static cylinder, namely $h(z,0) = 1$ and $u(z,0) = 0$.

4.3 Numerical procedure

To solve the equations (4.1)-(4.2) numerically, the method of lines described in Furlani & Hanchak (2011) has been implemented. Accordingly, the spatial derivatives are discretised using a second-order finite difference scheme, and the time derivatives can then be solved as a set of ordinary differential equations for the discretised radii and velocities.

Although the spatial domain evolves over time due to the plate movement, a fixed computational domain $0 \leq \xi \leq 1$ is used to ease the implementation of the spatial derivatives and also to avoid the need of an adaptative method. To that end, the instantaneous domain length is used as a rescaling parameter of the form $\xi = z/L(t)$. This mapping introduces in the equations (4.1)-(4.3) the metrics given by the chain rule which, for the i-th spatial derivative, reads $\partial_z^i = 1/L^i \partial_\xi^i$. The time derivatives are also modified, yielding $\partial_t = \partial_\tau - (v/L)\,\xi\,\partial_\xi$, being $\tau = t$ the computational time, which is not rescaled.

To increase the numerical stability of the method, two staggered grids are used for the computation of the radii and the velocities, as suggested by Furlani & Hanchak (2011). Thus, the local radius h is computed at n equidistant points

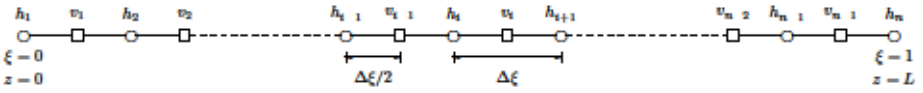

Figure 4.3: Staggered computational grid.

in the computational domain, while $n-1$ velocity nodes are uniformly placed interlaced midway between those defined for h as shown in Figure 4.3. The details of the discretisation can be found in Appendix B.

The temporal evolution is solved using Matlab® ode15s built-in function, which is a variable order, multistep, implicit solver, capable of handling stiff problems.

The code was tested using two particular cases, i.e. the static shape of a portion of fluid held captive between two plates, and the case of a stretching liquid bridge at a constant velocity (Zhang *et al.*, 1996), obtaining excellent agreement with the reference data in both cases. In addition, grid tests were performed to ensure independence of the numerical results on the discretisation. All the simulations reported in Section 4.4 are computed using $n = 200$, and the relative error in volume conservation is less than 0.6% for the reference case mentioned above. The number of timesteps is $n_t \sim 500$ to provide smooth evolutions of the shapes and velocity fields. With this set of parameters, the time needed to perform a simulation is less than 3 minutes in a standard desktop computer.

4.4 Results

4.4.1 Constant plate radius

The model proposed in the present work was validated by comparing the numerical results with the experiments performed in KU Leuven. To that end, one representative run of the 10PS20 suspension in PDMS2 was chosen as the reference case. Here, the values of the governing parameters are $Oh = 9.6$ and $Bo = 2.1 \times 10^{-3}$. In Figure 4.4(a) the velocity v, and the dimensionless inertia a_0/g are represented as a function of time to pinch-off $t_p - t$, for this case and the comparison between the numerically computed and the experimental evolution of the minimum radius of the stretching filament is plotted in Figure 4.4(b). From the results shown in Figure 4.4(b) it can be deduced that although the trend of the simulation is the same as in the experiment, obtaining a good

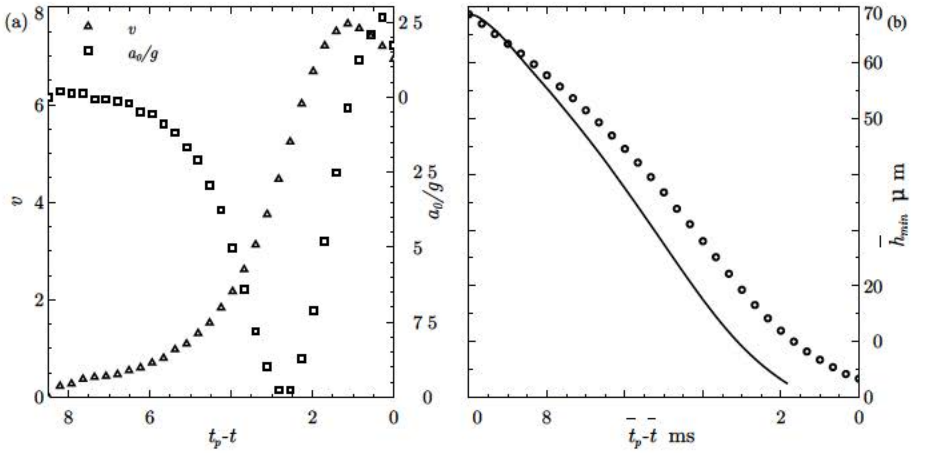

Figure 4.4: (a) Experimental velocity profile evolution, △ (left scale) and dimensionless inertia a_0/g, □ (right axis), as functions of over time to pinch-off $t_p - t$ used as input parameters for the model to calculate the case of 10% PS20 particles in PDMS oil with $\eta = 360$ mPa s. (b) Comparison of the numerical (solid line) and experimental (symbols) minimum radius for the same case.

qualitative agreement, there are differences in magnitude, leading to a faster pinching of the numerical solution.

The difference between the simulation and the experiment can be explained due to the assumptions made in the model. In particular, if the local filament radii at the end particle positions are carefully observed in Figure 4.1, it is clear that both decrease with time. Hence, the hypothesis of a constant plate size in the model seems an invalid assumption. The pinned contact line in a radius larger than in the real case implies that, for the same liquid volume, the hourglass-like shape of the bridge is more pronounced. In turn, this leads to a local thinning which is faster in the simulation than in experiment, as a result of the destabilizing effect that an increase of the radial curvature has in the filament due to an increased capillary pressure in the neck radius.

4.4.2 Linearly decreasing plate radius

To confirm that the origin of the quantitative disagreement between the simulation and the experiment is caused by the hypothesis of a constant radius of the end plates, the influence of a decreasing plate radius on the thinning dynamics has also been studied. To that end, the boundary conditions were modified,

imposing the simplest possible size time evolution, namely a linearly decreasing law. In dimensional variables, this corresponds to $R\left(\bar{t}\right) = R_0 - (R_f - R_0)\bar{t}/\bar{t}_p$, being R_f the plate radius when the filament pinches off, at time $\bar{t}_p$. The value of R_f can be roughly estimated as twice the particle radius.

In Figure 4.5(a), the evolution of the minimal radius over time is presented for the case with $R_f = 30$ μm. As can be observed, the decreasing size of the plates improves the agreement between the simulation and the experiment, demonstrating that the hypothesis of fixed boundary condition is too restrictive. Nevertheless, the use of such a simple law entails several drawbacks. At the early times, when the stretching velocity is small, the evolution of the minimum radius coincides with the instantaneous plate size, instead of the neck of the filament. Thus, the simulated shapes during these initial stages are more similar to a barrel than to an hourglass. The inset of Figure 4.5(a) shows a detail of the initial stage, in which a change in the slope of the computed evolution can be observed, corresponding to the unphysical result mentioned above. In addition, R_f is a free parameter of the model, whose value can be selected to improve the agreement between the numerical and experimental results. In summary, the minimum radius of the liquid bridge is better reproduced when considering that the end plates shrink with time, but the simplicity of a linearly decreasing law implies that the shape of the whole filament is not properly captured in all the spatial domain, specially near the ends. An example can be found in Figure 4.5(b).

4.4.3 Experimentally determined plate radius

To improve the agreement with the experiments, as well as to eliminate any free parameter, the model can be improved to simulate more realistic conditions. Thus, in the present section, instead of supposing a linear decrease of the plate radii, the real evolution of the radius at both ends, $\bar{h}(0,\bar{t}) = \bar{h}_{exp}(0,\bar{t})$ and $\bar{h}\left(\bar{L},\bar{t}\right) = \bar{h}_{exp}\left(\bar{L},\bar{t}\right)$ is imposed. As can be observed in Figure 4.6, where these the temporal evolutions are plotted for the reference case, the boundary conditions are far from being constant. Moreover, it can be appreciated that they are not equal for both plates, although its tendency is similar.

As can be observed in Figure 4.6, $\bar{h}(0,0) \neq \bar{h}\left(\bar{L},0\right)$, so the initial condition of a cylindrical shape used until this point is no longer valid. Therefore, the real shape of the filament extracted from the experiment has also been used as initial condition for the interface profile $\bar{h}\left(\bar{z},0\right) = \bar{h}_{exp}\left(\bar{z},0\right)$. With these new

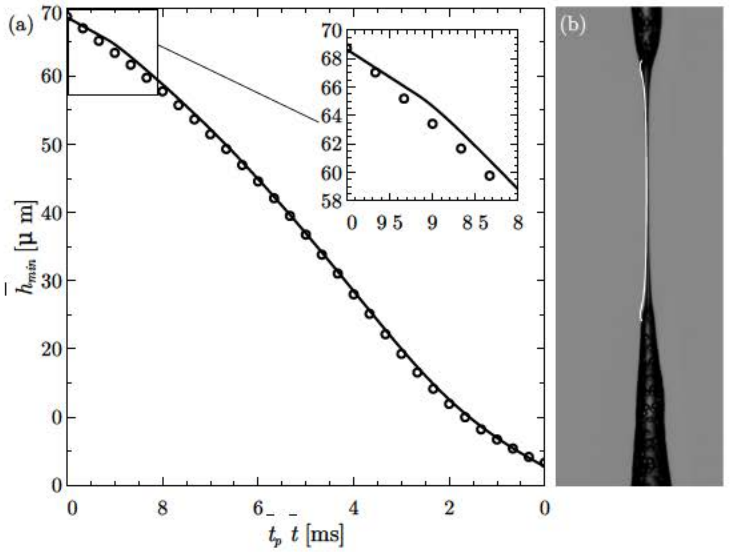

Figure 4.5: (a) Comparison between the time evolution of the experimental (symbols) and the numerical (solid line) minimum diameter for the reference case using a linearly decreasing size of the plates as a boundary condition with $R_f = 30$ μm. The inset shows a zoom of the initial instants. (b) Comparison between the computed and the experimental shape at $\bar{t}_p - \bar{t} = 1.0$ ms.

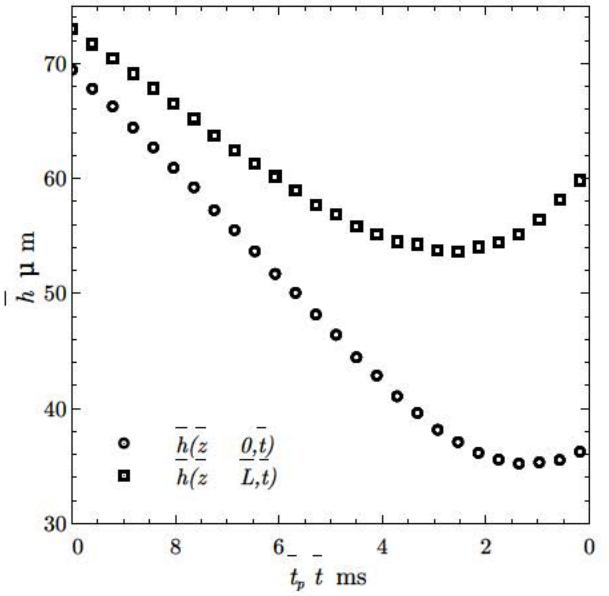

Figure 4.6: Temporal evolution of the experimental radii at the positions of the end particles in the reference case. Squares represent the top plate radius, and circles the bottom one.

boundary and initial conditions, the computed evolution of the neck radius is in excellent agreement with the experimental result for the reference case, as can be observed in Figure 4.7.

Moreover, this agreement remains very good when modifying the properties of the suspension. Indeed, in Figure 4.8, the comparison between numerical simulations and experiments is extended, presenting different cases when varying one property at a time while keeping the rest constant. Thus, the results are presented for two different particle concentrations, particle sizes and matrix viscosities, as summarized in Table 4.2.

With the change in the boundary condition, the model is not only able to predict the minimum radius between the two end particles, but also the shape of the whole filament. This fact can be observed in Figure 4.9, where the computed profiles are plotted over the experimental images, for the reference case of 10% PS particles of radius $R_p = 20$ μm in PDMS oil of viscosity $\eta = 360$ mPa s. In particular, it can be deduced from the agreement between the simulation and the experiment that the thinning and pinch-off of the suspension is Newtonian, and that the proposed one-dimensional model is appropriate to describe the

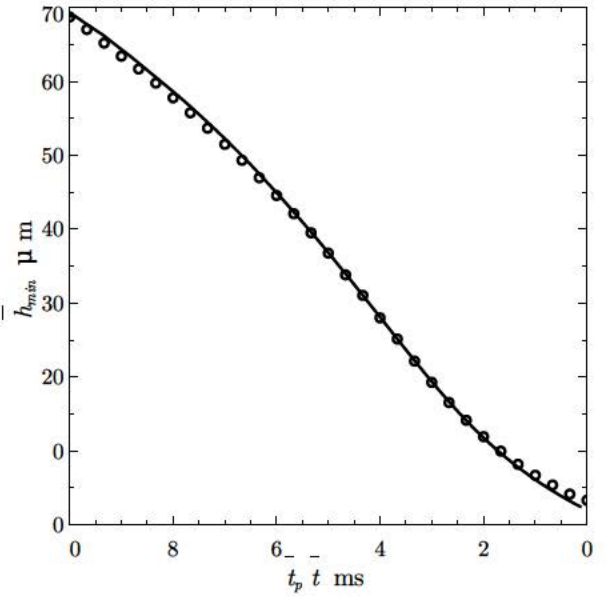

Figure 4.7: Temporal evolution of the minimum diameter for the case of 10% PS20 particles in PDMS oil $\eta = 360$ mPa s, using the experimental profile as initial condition, and the experimental evolutions of the end-plate radii as boundary conditions.

Variation	ϕ	R_p [μm]	Matrix
Reference	10%	20	PDMS 2
Concentration	25%	20	PDMS 2
Particle size	10%	10	PDMS 2
Matrix	10%	20	PDMS 1

Table 4.2: Variations from the reference suspension to extend the comparisons.

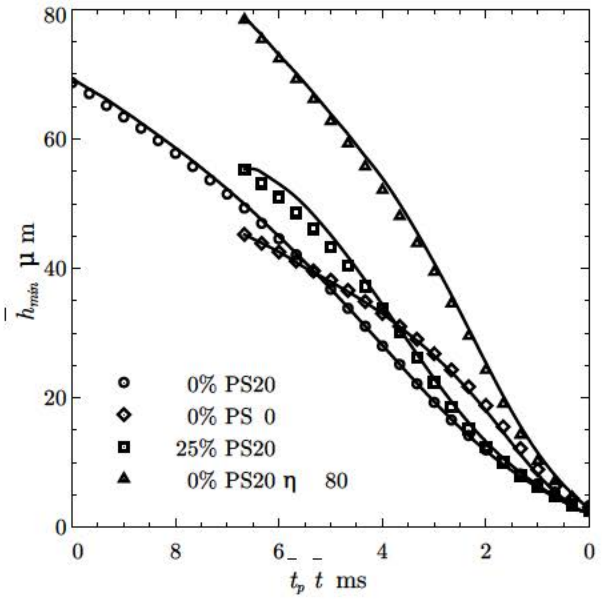

Figure 4.8: Comparison between the computed (lines) and experimental (symbols) evolution of the minimum diameter for different suspension properties. With ∘, the reference case of 10PS20 in PDMS 1; 10% particles of radius $R_p = 10$ μm in PDMS oil $\eta = 360$ mPa s, ◇; 25% PS particles of radius $R_p = 20$ μm in the same oil, □; and 10% PS particles of radius $R_p = 20$ μm in PDMS 2 oil, with $\eta = 180$ mPa s, △.

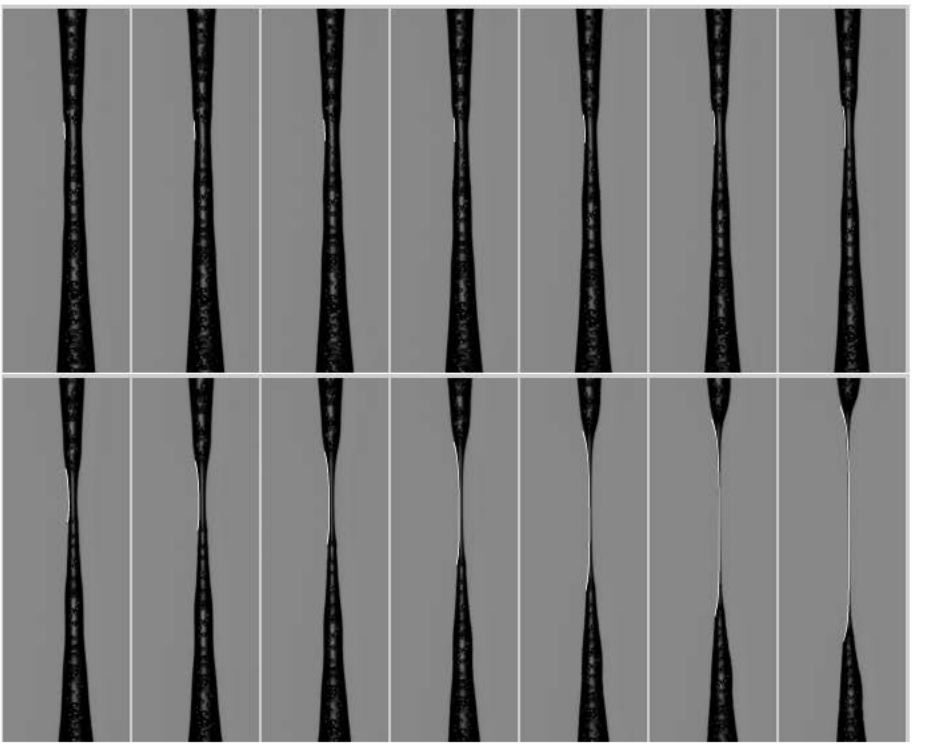

Figure 4.9: Experimental and numerical shape evolution comparisons for the case of 10% PS20 particles in PDMS oil $\eta = 360$ mPa s. The time between two consecutive frames is 0.666 ms.

thinning dynamics.

Figure 4.10 shows the comparisons between the simulations and experiments when varying the suspension properties. The dependence of the thinning velocities on the suspension properties were recently discussed by Mathues *et al.* (2015). The top row of Figure 4.10 shows the case of 10% concentration of particles with radius $R_p = 10$ μm in PDMS 2, the smaller size of the particles being clearly noticeable from the images. In the middle row the concentration is different than that of the reference case, namely 25% PS20 particles in silicone oil of viscosity $\eta = 360$ mPa s. Finally, the bottom row of Figure 4.10 shows the case of 10% PS20 particles in a silicone oil matrix with a different viscosity of $\eta = 180$ mPa s. In all cases, the simulations correctly predict the shape of the filament during the whole process, provided that the experimental stretching velocities and the radii at both ends are used as boundary conditions.

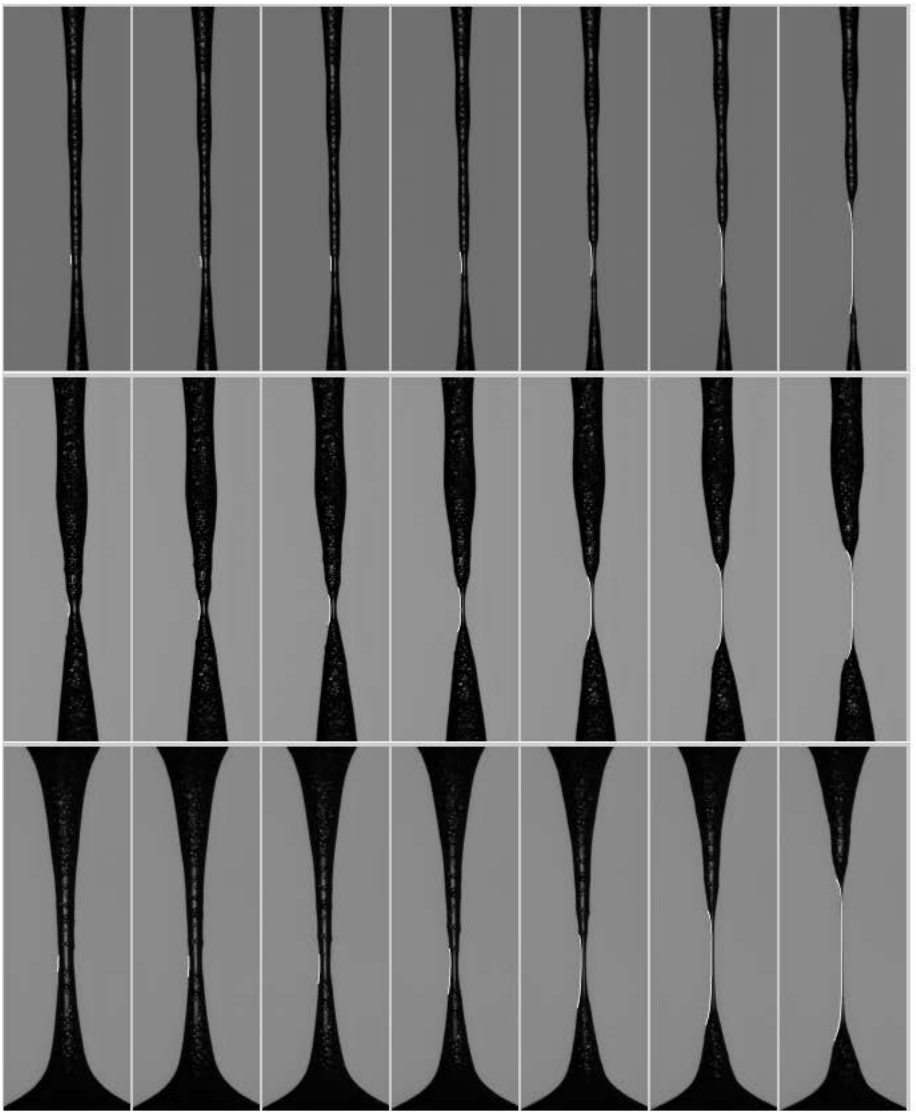

Figure 4.10: Comparison between the experimental and numerical shape evolution for the cases: 10% PS10 particles in PDMS oil $\eta = 360$ mPa s (top row); 25% PS20 particles in PDMS oil $\eta = 360$ mPa s (middle row); and 10% PS20 particles in PDMS oil $\eta = 180$ mPa s (bottom row). The time between two consecutive frames is 0.666 ms.

4.5 Conclusions

In this chapter a simple model to describe the final thinning stage of particulate suspensions has been developed. This final behaviour had not been correctly captured in previous studies, which only provided good descriptions of the thinning dynamics at earlier stages of the process. Considering the interstitial fluid between two end particles as a small-scale Newtonian liquid bridge, the one-dimensional mass and momentum equations due to Eggers & Dupont (1994) are capable of describing the shape evolution of the stretching filament, provided that the velocities and the radii at both ends extracted from the experiments are used as boundary conditions. The results are in excellent agreement with the experiments for different cases, including variations of the particle size, the concentration and the matrix viscosity. Moreover, the calculations involve an extremely low computational cost, running in a standard personal computer in a few minutes. The results obtained herein clearly demonstrate that the end pinching dynamics of a dilute particulate suspension, which rheologically constitutes a non-Newtonian system, corresponds to a Newtonian fluid break-up. However, these thinning and rupture differ qualitatively from the evolution of a destabilized Newtonian liquid bridge between two fixed plates, since the non-uniform movement of the end particles adds an active stretching mechanism, apart from the capillary pressure driven thinning.

Once demonstrated in this chapter the convenience of the proposed model to describe the dynamics, a natural extension of this work would be to derive a predictive model. Thus, if both the velocities of the tracked end particles, and the time evolution of the filament radii at these positions could be predicted as functions of the properties of the suspension, the simulations performed in this work would turn independent of the experiments. This modelling effort would have to deal with the non-Newtonian behaviour of the colloidal suspensions, which is out of the scope of this Thesis. However, the model presented here could be used in its current state to study the detailed thinning and break-up of stretched foam filaments, in those cases where the pinch-off event occurs in a liquid bridge stretched between two bubbles. Finally, another line of interest deals with possible phase transitions taking place during the stretching process of the bridge. As a prominent example, the heat transfer with the environment causes the solidification of lava filaments in volcanic eruptions (Villermaux, 2012). Based on this interesting natural phenomena, one can envision practical applications where the formation of micrometric solid strands is controlled

thanks to the interplay between axial stretching and radial heat transfer.

References

Bonnoit, C., Bertrand, T., Clément, E. & Lindner, A. 2012 Accelerated drop detachment in granular suspensions. *Phys. Fluids* 24, 043304.

Brertrand, T., Bonnoit, C., Clement, E. & Lindner, A. 2012 Dynamics of drop formation in granular suspensions: The role of volume fraction. *Grannular Matter* 14, 169–174.

Eggers, J. & Dupont, T. F. 1994 Drop formation in a one-dimensional approximation of the navier-stokes equation. *J. Fluid Mech.* 262, 205–222.

Furbank, R. J. & Morris, J. F. 2004 An experimental study of particle effects on drop formation. *Phys. Fluids* 16, 1777–1790.

Furbank, R. J. & Morris, J. F. 2007 Pendant drop thread dynamics of particle-laden liquids. *Int. J. Multiphase Flow* 33, 448–468.

Furlani, E. P. & Hanchak, M. S. 2011 Nonlinear analysis of the deformation and breakup of viscous microjets using the method of lines. *Int. J. Numer. Meth. Fluids* 65, 563–577.

Lidner, A., Fiscina, J. E. & Wagner, C. 2015 Single particles accelerate final stages of capillary break-up. *Europhys. Lett.* 110, 64002.

Mathues, W. 2015 Filament stabilisation in free-surface flows of complex fluids. PhD thesis, KU Leuven.

Mathues, W., McIlroy, C., Harlen, O. G. & Clasen, C. 2015 Capillary breakup of suspensions near pinch-off. *Phys. Fluids* 27, 093301.

McIlroy, C. & Harlen, O. G. 2014 Modelling capillary breakup of particulate suspensions. *Phys. Fluids* 26, 033101.

Nicolas, M. 2002 Experimental study of gravity-driven dense suspension jets. *Phys. Fluids* 14, 3570–3576.

Van Deen, M. S., Bertrand, T., Vu, N., Quéré, D., Clement, E. & Lidner, A. 2013 Particles accelerate the detachment of viscous liquids. *Rheol. Acta* 52, 403–412.

Villermaux, E. 2012 The formation of filament structures from molten silicates: Pele's hair, angel hair, and blown clinker. *C. R. Mecanique* 340, 555–564.

Zhang, X., Padgett, R. S. & Basaran, O. A. 1996 Nonlinear deformation and breakup of stretching liquid bridges. *J. Fluid Mech.* 329, 207–245.

Zhao, H., Liu, H. F., Xu, J. L., Li, W. F. & Lin, K. F. 2015 Inhomogeneity in breakup of suspensions. *Phys. Fluids* 27, 063303.

CHAPTER
FIVE

Concluding remarks and future prospects

5.1 Conclusions and summary of the results

In this dissertation, several new linear and non-linear phenomena of practical relevance in the context of extensional capillary flows have been studied. The approach combines experimental, theoretical and numerical tools aimed to properly account for the competing mechanisms present in these flows, namely inertia, surface tension and viscous forces, under the presence of axial stretching.

The results presented in this Ph.D. Thesis can be summarized according to the different tasks accomplished by this point. From a theoretical point of view, clear definitions of the different problems and their mathematical modelling, as well as their numerical solution by developing home-made tools have been successfully accomplished. To perform the experiments, the design, construction and set-up of an experimental facility has also been necessary.

It is important to emphasize that the choice of the one-dimensional model for the theoretical description allows to achieve accurate predictions despite its simplicity, with a very little computational cost compared to full Navier-Stokes simulations. In addition, this simplicity is undoubtedly an advantage to understand the underlying physics, compared to more intricate models.

The experimental work performed has allowed to check the validity of the developed models and, in those cases where modelling has not been accomplished, the experimental result obtained were the only vehicle to show the dynamics, apart from revealing new phenomena.

In the first part of the Thesis, a global linear stability analysis of freely falling liquid jets has been performed. The work, both theoretical and experimental, shows the accuracy of the one-dimensional model to describe the transition to dripping, provided that the exact expression of the interfacial curvature is retained. Indeed, the consideration of the axial curvature has been crucial for the analysis, and has revealed its central role in stabilizing the highly stretched

liquid thread. The model developed has been shown to provide much better agreement with the experimental jetting to dripping transition events than those available in the literature (Sauter & Buggisch, 2005). In particular, the results surprisingly reveal that, at a certain point far from the outlet, a thinner steady thread can be obtained by increasing the injector radius.

In the second part, which deals with the fully non-linear phenomena present in the dripping dynamics, an extensive experimental work has been performed. The influence of the injector diameter both on the dripping dynamics and on the transition to jetting has been characterized through new experiments, covering unexplored regions of the governing parameter space. These experimental results have been summarized in new phase diagrams and reveal the failure of the previously available scaling laws (Ambravaneswaran *et al.*, 2004) to predict the jetting transition, when the Bond number is increased. Moreover, the experiments carried out in the first part of the work have allowed to quantify for the first time the hysteresis present in the jetting transition in the case of a liquid different from water. Finally, the finding of new regimes with satellite drops not previously reported has to be highlighted, thanks to the use of injectors of large enough diameters.

The last part of the dissertation confirms the capabilities of the one-dimensional mass and momentum conservation equations to describe the type of extensional flows considered in this work. While in the first part of the Thesis the one-dimensional model was used to predict the global linear stability properties of a gravitationally-stretched liquid thread, in the last part the non-linear deformation and break-up of a stretching filament is modelled using the same system of equations, obtaining again an excellent agreement with the experimental results. The latter model, resulting from the need to improve the understanding on how particulate suspensions thin and break (Mathues *et al.*, 2015), demonstrates that the last stages of the pinching dynamics correspond to a Newtonian behaviour of the interstitial fluid trapped between two end particles, that effectively act as boundaries with a time varying velocity. The results of the model were compared with different set of experiments and confirm the convenience of the one-dimensional equations even when dealing with non-linear phenomena.

5.2 Outlook for future research

Although future works related to each specific part of the dissertation have been already introduced in the corresponding chapters, the main lines are summarized here for completeness.

The long-term dynamics of globally unstable jets cannot be predicted with the linear stability analysis presented in the first part of the Thesis. However, once the capability of the one-dimensional equations to describe also non-linear behaviours has been demonstrated in the last part of the dissertation, the study of the conditions determining whether the self-excited oscillations either grow in time or evolve towards a limit cycle deserves a future study.

Another line of interest is the use of fluids with non-Newtonian rheologies, or with modified properties as in the practically important case of surfactant addition. Indeed, if the constitutive law of the working fluid does not require the introduction of a relaxation time, the linear stability analysis can be straightforwardly applied. Thus, it would be of interest to consider generalized Newtonian fluids, using the strain-thinning behaviour as a starting point.

Finally, the work on stretching liquid bridges can be extended along two different paths. The first one would be the detailed study of foam thinning and break-up, and check the validity of a model consisting of a liquid bridge being stretched between two bubbles. The second proposed line of research would deal with the problem of coupling heat transfer and phase transition phenomena with the stretching scenario, leading to liquid bridges that may solidify during or after the thinning and break-up processes.

References

Ambravaneswaran, B., Subramani, H. J., Phillips, S. D. & Basaran, O. A. 2004 Dripping-jetting transitions in a dripping faucet. *Phys. Rev. Lett.* 93, 034501.

Mathues, W., McIlroy, C., Harlen, O. G. & Clasen, C. 2015 Capillary breakup of suspensions near pinch-off. *Phys. Fluids* 27, 093301.

Sauter, U. S. & Buggisch, H. W. 2005 Stability of initially slow viscous jets driven by gravity. *J. Fluid Mech.* 533, 237–257.

APPENDIX

A

Spectral discretisation

The equation (2.20) and the system (2.25) are discretised with a spectral Chebyshev collocation method. Since the jet domain is $0 \leq z \leq L$, while Chebyshev nodes are defined in $-1 \leq y \leq 1$, it is necessary to define a proper mapping to represent the physical domain. The particular mapping chosen in this work is given by equation (2.34), and reproduced here for completeness,

$$z = \frac{bL(1+y)}{2b + L(1-y)}. \tag{A.1}$$

The metrics introduced by the use of the mapping (A.1) can be easily calculated, and for the i-th derivative read

$$\frac{\partial^i y}{\partial z^i} = (-1)^{i+1} 2i! \frac{b(b+L)}{L(b+z)^{i+1}}. \tag{A.2}$$

Thus, derivatives in physical space can be obtained by applying the chain rule,

$$\frac{\partial}{\partial z} = \frac{\partial y}{\partial z} D_1, \tag{A.3}$$

$$\frac{\partial^2}{\partial z^2} = \frac{\partial^2 y}{\partial z^2} D_1 + \left(\frac{\partial y}{\partial z}\right)^2 D_2, \tag{A.4}$$

$$\frac{\partial^3}{\partial z^3} = \frac{\partial^3 y}{\partial z^3} D_1 + 3\frac{\partial^2 y}{\partial z^2}\frac{\partial y}{\partial z} D_2 + \left(\frac{\partial y}{\partial z}\right)^3 D_3, \tag{A.5}$$

where D_1, D_2 and D_3 are the first, second and third order Chebyshev differentiation matrices respectively, discussed in detail in Weideman & Reddy (2000).

References

Weideman, J.A.C. & Reddy, S.C. 2000 A matlab differentiation matrix suite. *ACM Trans. Math. Soft.* 26, 465–519.

APPENDIX

B

Finite difference discretisation

The continuity equation (4.1) is computed at the n points corresponding to the local radius grid ξ_i^h. Taking into account the metrics introduced by the mapping, explained in Section 4.3, the discretised continuity equation reads

$$2h_i \frac{\mathrm{d}h_i}{\mathrm{d}\tau} = -\frac{1}{L} \left.\frac{\partial(h^2 u)}{\partial \xi}\right|_{\xi_i^h} + \frac{v}{L} \xi_i^h \left.\frac{\partial h^2}{\partial \xi}\right|_{\xi_i^h}, \tag{B.1}$$

where

$$\left.\frac{\partial(h^2 u)}{\partial \xi}\right|_{\xi_i^h} = \frac{u_i h_{i+1/2}^2 - u_{i-1} h_{i-1/2}^2}{\Delta \xi} \tag{B.2}$$

and

$$\left.\frac{\partial h^2}{\partial \xi}\right|_{\xi_i^h} = \frac{h_{i+1/2}^2 - h_{i-1/2}^2}{\Delta \xi} \tag{B.3}$$

with $h_{i+1/2} = (h_i + h_{i+1})/2$ and $h_{i-1/2} = (h_i + h_{i-1})/2$, yielding

$$\frac{\mathrm{d}h_i}{\mathrm{d}\tau} = \frac{(h_{i+1} + h_i)^2 (v\xi_i^h - u_i) - (h_i + h_{i-1})^2 (v\xi_i^h - u_i)}{8L\Delta\xi h_i}, \tag{B.4}$$

for $i = 2, \ldots, n-1$. Note that $h_1 = h(z = 0)$ and $h_n = h(z = L)$ correspond to the boundary conditions, which are known.

The momentum equation (4.2) is discretised at the $n-1$ nodes of the velocity grid ξ_i^u, after applying the chain rule to convert the physical domain into the numeric one:

$$\begin{aligned} \frac{\mathrm{d}u_i}{\mathrm{d}\tau} =& \frac{v}{L} \xi_i^u \left.\frac{\partial u}{\partial \xi}\right|_{\xi_i^u} - \frac{1}{L} u \left.\frac{\partial u}{\partial \xi}\right|_{\xi_i^u} - Oh^2 \frac{1}{L} \left.\frac{\partial \mathcal{C}}{\partial \xi}\right|_{\xi_i^u} + \\ &+ 3Oh^2 \frac{1}{h^2} \frac{1}{L} \frac{\partial}{\partial \xi} \left(h^2 \frac{1}{L} \frac{\partial u}{\partial \xi} \right) \Bigg|_{\xi_i^u} - Oh^2 Bo \left(1 + \frac{a_0}{g} \right). \end{aligned} \tag{B.5}$$

The advection terms in equation (B.5) are discretised using an upwinding scheme,

$$\frac{v}{L}\xi_i^u \left.\frac{\partial u}{\partial \xi}\right|_{\xi_i^u} - \frac{1}{L}\, u \left.\frac{\partial u}{\partial \xi}\right|_{\xi_i^u} = -\frac{1}{L}\left(u^+ d^- + u^- d^+\right), \tag{B.6}$$

being $u^+ = \max\{u_i - v\xi_i^u, 0\}$, $u^- = \min\{u_i - v\xi_i^u, 0\}$, $d^- = (u_i - u_{i-1})/\Delta\xi$ and $d^+ = (u_{i+1} - u_i)/\Delta\xi$.

The pressure term, corresponding to the curvature gradient, results in

$$\left.\frac{\partial \mathcal{C}}{\partial \xi}\right|_{\xi_i^u} = \frac{\mathcal{C}_{i+1} - \mathcal{C}_i}{\Delta\xi}, \tag{B.7}$$

where

$$\mathcal{C}_i = \frac{1}{h_i A_i^{1/2}} - \frac{h_{i+1} - 2h_i + h_{i-1}}{2L^2\Delta\xi^2 A_i^{3/2}}. \tag{B.8}$$

being

$$A_i = \begin{cases} 1 + \left(\dfrac{-3h_1 + 4h_2 - h_3}{2L\Delta\xi}\right)^2, & \text{for } i = 1 \\ 1 + \left(\dfrac{h_{i+1} - h_{i-1}}{2L\Delta\xi}\right)^2, & \text{for } i = 2, \ldots, n-1 \\ 1 + \left(\dfrac{h_{n-2} - 4h_{n-1} + 3h_n}{2L\Delta\xi}\right)^2, & \text{for } i = n. \end{cases} \tag{B.9}$$

The viscous contribution reads

$$\frac{1}{h^2}\frac{\partial}{\partial \xi}\left(h^2 \frac{\partial u}{\partial \xi}\right)\bigg|_{\xi_i^u} = \frac{1}{h_{i+1/2}^2} \frac{h_{i+1}^2 \left.\frac{\partial u}{\partial \xi}\right|_{\xi_{i+1/2}^u} - h_{i-1}^2 \left.\frac{\partial u}{\partial \xi}\right|_{\xi_{i-1/2}^u}}{\Delta\xi} \tag{B.10}$$

with

$$\begin{aligned} \left.\frac{\partial u}{\partial \xi}\right|_{\xi_{i+1/2}^u} &= \frac{u_{i+1} - u_i}{\Delta\xi}, \\ \left.\frac{\partial u}{\partial \xi}\right|_{\xi_{i-1/2}^u} &= \frac{u_i - u_{i-1}}{\Delta\xi}, \end{aligned} \tag{B.11}$$

yielding

$$\frac{1}{h^2}\frac{\partial}{\partial \xi}\left(h^2 \frac{\partial u}{\partial \xi}\right)\bigg|_{\xi_i^u} = \frac{4}{(h_{i+1} + h_i)^2} \frac{h_{i+1}^2(u_{i+1} - u_i) - h_i^2(u_i - u_{i-1})}{\Delta\xi^2}. \tag{B.12}$$

Thus, the discretised momentum equation reads

$$\begin{aligned} \frac{\mathrm{d}u_i}{\mathrm{d}\tau} = &-\frac{1}{L}\left(u^+ d^- + u^- d^+\right) - Oh^2 \frac{\mathcal{C}_{i+1} - \mathcal{C}_i}{L\Delta\xi} + \\ &+ 12Oh^2 \frac{h_{i+1}^2(u_{i+1} - u_i) - h_i^2(u_i - u_{i-1})}{L^2\Delta\xi^2(h_{i+1} + h_i)^2} - Oh^2 Bo\left(1 + \frac{a_0}{g}\right), \end{aligned} \tag{B.13}$$

for $i = 1, \ldots, n-1$.

In the cases $i = 1$ and $i = n$, the values of the velocities in two ghost nodes, namely u_0 and u_n are needed. These values can be calculated imposing the boundary conditions, taking into account that those are known in nodes that do not belong to the grid in the case of the velocity. Hence, $u(z = 0) = u_{1/2} = (u_0 + u_1)/2 = 0$, giving $u_0 = -u_1$. Similarly, $u(z = L) = u_{n-1/2} = (u_{n-1} + u_n)/2 = v$, so that $u_n = 2v - u_{n-1}$.

Alphabetical list of references

References

Ambravaneswaran, B., Subramani, H. J., Phillips, S. D. & Basaran, O. A. 2004 Dripping-jetting transitions in a dripping faucet. *Phys. Rev. Lett.* 93, 034501.

Ambravaneswaran, B., Wilkes, E. D. & Basaran, O. A. 2002 Drop formation from a capillary tube: Comparison of one-dimensional and two-dimensional analyses and occurrence of satellite drops. *Phys. Fluids* 14, 2606–2621.

Barrero, A. & Loscertales, I. G. 2007 Micro- and nanoparticles via capillary flows. *Annu. Rev. Fluid Mech.* 39, 89–106.

Basaran, O. A., Gao, H. J. & Bhat, P. P. 2013 Nonstandard inkjets. *Annu. Rev. Fluid Mech.* 45, 85–113.

Bhat, P. P., Appathurai, S., Harris, M. T., Pasquali, M., McKinley, G. H. & Basaran, O. A. 2010 Formation of beads-on-a-string structures during break-up of viscoelastic filaments. *Nature* 6, 625–631.

Bonnoit, C., Bertrand, T., Clément, E. & Lindner, A. 2012 Accelerated drop detachment in granular suspensions. *Phys. Fluids* 24, 043304.

Brenner, M. P., Eggers, J., Joseph, K., Nagel, S. R. & Shi, X. D. 1997 Breakdown of scaling in high Reynolds number droplet fission. *Phys. Fluids* 9, 1573–1590.

Brertrand, T., Bonnoit, C., Clement, E. & Lindner, A. 2012 Dynamics of drop formation in granular suspensions: The role of volume fraction. *Grannular Matter* 14, 169–174.

Briggs, R. J. 1964 *Electron-stream interaction with plasmas (Research monograph no. 29)*. MIT Press.

Canuto, C., Hussaini, M. Y., Quarteroni, A. & Zang, T. A. 2006 *Spectral methods. Fundamentals in single domains*. Springer-Verlag.

Castrejón-Pita, A. A., Castrejón-Pita, J. R. & Hutchings, I. M. 2012 Breakup of liquid filaments. *Phys. Rev. Lett.* 108, 074506.

Chen, X. B. 2009 Modeling and control of fluid dispensing prprocess: A state of the art review. *Int. J. Adv. Manuf. Technol.* 43, 276–286.

Clanet, C. & Lasheras, J. C. 1999 Transition from dripping to jetting. *J. Fluid Mech.* 383, 307–326.

Clasen, C., Bico, J., Entov, V. M. & McKinley, G. H. 2009 'Gobbling drops': the jetting–dripping transition in flows of polymer solutions. *J. Fluid Mech.* 636, 5–40.

Clasen, C., Phillips, P. M., Palangetic, L. & Vermant, J. 2012 Dispensing of rheologically complex fluids: The map of misery. *AIChE J.* 58, 3242–3255.

Consoli-Lizzi, P., Coenen, W. & Sevilla, A. 2014 Experiments and non-parallel theory on the natural break-up of freely falling newtonian liquid jets. In *Bulletin of the American Physical Society*, , vol. 59, pp. 244–245.

Coullet, P., Mahadevan, L. & Riera, C. S. 2005 Hydrodynamical models for the chaotic dripping faucet. *J. Fluid Mech.* 526, 1–17.

Denn, M. M. 1980 Continuous drawing of liquids to form fibers. *Annu. Rev. Fluid Mech.* 12, 365–387.

Doshi, J. & Reneker, D. H. 1995 Electrospinning process and applications of electrospun fibers. *J. Electrostatics* 35, 151–160.

Driessen, T., Jeurissen, R., Wijshoff, H., Toschi, F. & Loshe, D. 2013 Stability of viscous long liquid filaments. *Phys. Fluids* 25, 062109.

Duchemin, L., Dizès, S. Le, Vincent, L. & Villermaux, E. 2015 Self-similar impulsive capillary waves on a ligament. *Phys. Fluids* 27, 051704.

Eggers, J 1997 Nonlinear dynamics and breakup of free surface flows. *Rev. Mod. Phys.* 69, 865–929.

Eggers, J. & Dupont, T. F. 1994 Drop formation in a one-dimensional approximation of the navier-stokes equation. *J. Fluid Mech.* 262, 205–222.

Eggers, J. & Villermaux, E. 2008 Physics of liquid jets. *Rep. Prog. Phys.* 71, 036601.

Frankel, I. & Weihs, D. 1985 Stability of a capillary jet with linearly increasing axial velocity (with application to shaped charges). *J. Fluid Mech.* 155, 289–307.

Furbank, R. J. & Morris, J. F. 2004 An experimental study of particle effects on drop formation. *Phys. Fluids* 16, 1777–1790.

Furbank, R. J. & Morris, J. F. 2007 Pendant drop thread dynamics of particle-laden liquids. *Int. J. Multiphase Flow* 33, 448–468.

Furlani, E. P. & Hanchak, M. S. 2011 Nonlinear analysis of the deformation and breakup of viscous microjets using the method of lines. *Int. J. Numer. Meth. Fluids* 65, 563–577.

Gañán-Calvo, A. M. 1998 Generation of steady liquid microthreads and micron-sized monodisperse sprays in gas streams. *Phys. Rev. Lett.* 80 (2), 285–288.

García, F. J. & Castellanos, A. 1994 One-dimensional models for slender axisymmetric viscous liquid jets. *Phys. Fluids* 6 (8), 2676–2689.

García, F. J., González, H., Castrejón-Pita, J. R. & Castrejón-Pita, A. A. 2014 The breakup length of harmonically stimulated capillary jets. *Appl. Phys. Lett.* 105, 094104.

Gaudet, S., McKinley, G. H. & Stone, H. A. 1994 Extensional deformation on newtonian and non-newtonian liquid bridges in microgravity. *AIAA* 94, 1–9.

Gordillo, J. M., Sevilla, A. & Campo-Cortés, F. 2014 Global stability of stretched jets: conditions for the generation of monodisperse micro-emulsions using coflows. *J. Fluid Mech.* 738, 335–357.

Guerrero, J., González, H. & García, F. J. 2012 Spatial modes of capillary jets, with application to surface stimulation. *J. Fluid Mech.* 702, 354–377.

Hoath, S. D., Hsiao, W. K., Hutchings, I. M. & Tuladhar, T. R. 2014 Jetted mixtures of particle suspensions and resins. *Phys. Fluids* 26, 101701.

Hoath, S. D., Jung, S. & Hutchings, I. M. 2013 A simple criterion for filament break-up in drop-on-demand inkjet printing. *Phys. Fluids* 25, 021701.

Hoepffner, J. & Paré, G. 2013 Recoil of a liquid filament: escape from pinch-off through creation of a vortex ring. *J. Fluid Mech.* 734, 183–197.

Huerre, P. & Monkewitz, P. A. 1985 Absolute and convective instabilities in free shear layers. *J. Fluid Mech.* 159, 151–168.

Keller, J. B., Rubinow, S. I. & Tu, Y. O. 1972 Spatial instability of a jet. *Phys. Fluids* 16, 2052–2055.

Kroger, R. & Rath, H. J. 1995 Velocity and elongation rate distributions in stretched polymeric and newtonian liquid bridges. *J. Non-Newtonian Fluid Mech.* 57, 137–153.

Landau, L.D. 1946 On the vibrations of the electronic plasma. *J. Phys. U.S.S.R.* 10 (25), 445–460.

Le Dizès, S. 1997 Global modes in falling capillary jets. *Eur. J. Mech. B/Fluids* 16, 761–778.

Leib, S. J. & Goldstein, M. E. 1986 The generation of capillary instabilities on a liquid jet. *J. Fluid Mech.* 168, 479–500.

Liao, Y. C., Franses, E. I. & Basaran, O. A. 2006 Deformation and breakup of a stretching liquid bridge covered with an insoluble surfactant monolayer. *Phys. Fluids* 18, 022101.

Liao, Y. C., Subramani, H. J., Franses, E. I. & Basaran, O. A. 2004 Effects of soluble surfactants on the deformation and breakup of stretching liquid bridges. *Lagmuir* 20, 9926–9930.

Lidner, A., Fiscina, J. E. & Wagner, C. 2015 Single particles accelerate final stages of capillary break-up. *Europhys. Lett.* 110, 64002.

Loscertales, I. G., Barrero, A., Guerrero, I., Cortijo, R., Marquez, M. & Gañán-Calvo, A. M. 2002 Micro/nano encapsulation via electrified coaxial liquid jets. *Science* 295, 1695–1698.

Marín, A. G., Campo-Cortés, F. & Gordillo, J. M. 2009 Generation of micron-sized drops and bubbles through viscous coflows. *Colloid Surface A* 344, 2–7.

Marín, A. G., Loscertales, I. G., Marquez, M. & Barrero, A. 2007 Simple and double emulsions via coaxial jet electrosprays. *Phys. Rev. Lett.* 98, 014502.

Marmottant, P. & Villermaux, E. 2004*a* Fragmentation of stretched liquid ligaments. *Phys. Fluids* 16, 2732.

Marmottant, P. & Villermaux, E. 2004*b* On spray formation. *J. Fluid Mech.* 498, 73–111.

Mathues, W. 2015 Filament stabilisation in free-surface flows of complex fluids. PhD thesis, KU Leuven.

Mathues, W., McIlroy, C., Harlen, O. G. & Clasen, C. 2015 Capillary breakup of suspensions near pinch-off. *Phys. Fluids* 27, 093301.

McIlroy, C. & Harlen, O. G. 2014 Modelling capillary breakup of particulate suspensions. *Phys. Fluids* 26, 033101.

McKinley, G. H. 2005 Visco-elasto-capillary thinning and break-up of complex fluids. *Rheol. Rev.* 3, 1–48.

McKinley, G. H. & Sridhar, T. 2002 Filament-stretching rheometry of complex fluids. *Annu. Rev. Fluid Mech.* 34, 375–415.

McKinley, G. H. & Tripathi, A. 2000 How to extract the Newtonian visosity from Capillary Breakup Measurements in a filament rheometer. *J. Rheol.* 44, 653–671.

Meseguer, J., Perales, J. M., Martínez, I. & Sanz, N. A. Bezdenejnykh A. 1999 'Hydrostatic instabilities' in floating zone crystal growth process. *Curr. Top. Cryst. Growth Res.* 5, 27–42.

Montanero, J. M., Herrada, M. A., Ferrera, C., Vega, E. J. & Gañán-Calvo, A. M. 2011 On the validity of a universal solution of viscous capillary jets. *Phys. Fluids* 23, 122103.

Nicolas, M. 2002 Experimental study of gravity-driven dense suspension jets. *Phys. Fluids* 14, 3570–3576.

Notz, P. K. & Basaran, O. A. 2004 Dynamics and breakup of a contracting liquid filament. *J. Fluid Mech.* 512, 223–256.

Notz, P. K., Chen, A. U. & Basaran, O. A. 2001 Satellite drops: Unexpected dynamics and change of scaling during pinch-off. *Phys. Fluids* 13, 549.

Pearson, J. R. A. & Matovich, M. A. 1969 Spinning a molten threadline. *I&EC fundamentals* 8, 605–609.

Perales, J. M. & Vega, J. M. 2011 Dynamics of nearly unstable axisymmetric liquid bridges. *Phys. Fluids* 23, 012107.

Peregrine, D. H., Shoker, G. & Symon, A. 1990 The bifurcation of liquid bridges. *J. Fluid Mech.* 212, 25.

Plateau, J. 1873 *Statique Expérimentale et Théorique des Liquides*. Gauthier-Villars et C^{ie}, Paris.

Rayleigh, W. S. 1878 On the instability of jets. *Proc. London Math. Soc.* 10, 4–13.

Reis, P. M., Jung, S., Aristoff, J. M. & Stocker, R. 2010 How cats lap: Water uptake by Felix catus. *Science* 330, 1231–1234.

Rodríguez-Rodríguez, J., Sevilla, A., Martínez-Bazán, C. & Gordillo, J. M. 2015 Generation of microbubbles with applications to industry and medicine. *Annu. Rev. Fluid Mech.* 47, 405–429.

Sauter, U. S. & Buggisch, H. W. 2005 Stability of initially slow viscous jets driven by gravity. *J. Fluid Mech.* 533, 237–257.

Schulkes, R. M. S. M. 1994 The evolution and bifurcation of a pendant drop. *J. Fluid Mech.* 278, 83–100.

Senchenko, S. & Bohr, T. 2005 Shape and stability of a viscous thread. *Phys. Rev. E* 71, 056301.

Sevilla, A. 2011 The effect of viscous relaxation on the spatiotemporal stability of capillary jets. *J. Fluid Mech.* 684, 204–226.

Shaw, R. 1984 *The dripping faucet as a model chaotic system*. Santa Cruz, CA: Aerial Press.

Shi, X. D., Brenner, M. P. & Nagel, S. R. 1994 A cascade of structure in a drop falling from a faucet. *Science* 265, 219–222.

Stokes, Y. M., Buchak, P., Crowdy, D. G. & Ebendorff-Heidepriem, H. 2014 Drawing of micro-structured fibres: circular and non-circular tubes. *J. Fluid Mech.* 755, 176–203.

Subramani, H. J., Yeoh, H. K., Suryo, R., Xum, Q., Ambravaneswaran, B. & Basaran, O. A. 2006 Simplicity and complexity in a dripping faucet. *Phys. Fluids* 18, 032106.

Suñol, F. & González-Cinca, R. 2015 Liquid jet breakup and subsequent droplet dynamics under normal gravity and in microgravity conditions. *Phys. Fluids* 27, 077102.

Tomotika, S. 1936 Breaking up of a drop of viscous liquid immersed in another viscous fluid which is extending at a uniform rate. *Proc. Roy. Soc.* 153, 302–318.

Umemura, A. & Osaka, J. 2014 Self-destabilizing loop observed in a jetting-to-dripping transition. *J. Fluid Mech.* 752, 184.

Van Deen, M. S., Bertrand, T., Vu, N., Quéré, D., Clement, E. & Lidner, A. 2013 Particles accelerate the detachment of viscous liquids. *Rheol. Acta* 52, 403–412.

Vega, E. J., Montanero, J. M., Herrada, M. A. & Ferrera, C. 2014 Dynamics of an axisymmetric liquid bridge close to the minimum-volume stability limit. *Phys. Rev. E* 90, 013015.

Villermaux, E. 2007 Fragmentation. *Annu. Rev. Fluid Mech.* 39, 419–446.

Villermaux, E. 2012 The formation of filament structures from molten silicates: Pele's hair, angel hair, and blown clinker. *C. R. Mecanique* 340, 555–564.

Villermaux, E., Pistre, V. & Lhuissier, H. 2013 The viscous Savart sheet. *J. Fluid Mech.* 730, 607–625.

Vincent, L., Duchemin, L. & Le Dizès, S. 2014*a* Forced dynamics of a short viscous liquid bridge. *J. Fluid Mech.* 761, 220–240.

Vincent, L., Duchemin, L. & Villermaux, E. 2014*b* Remnants from fast liquid withdrawal. *Phys. Fluids* 26, 031701.

Weideman, J.A.C. & Reddy, S.C. 2000 A matlab differentiation matrix suite. *ACM Trans. Math. Soft.* 26, 465–519.

Wilkes, E. D., Phillips, S. D. & Basaran, O. A. 1999 Computational and experimental analysis of dynamics of drop formation. *Phys. Fluids* 11, 3577–3598.

Yildirim, O. E. & Basaran, O. A. 2001 Deformation and breakup of stretching bridges of newtonian and shear-thinning liquids: comparison of one- and two-dimensional models. *Chem. Eng. Sci.* 56, 211–233.

Yildirim, O. E., Xu, Q. & Basaran, O. A. 2005 Analysis of the drop weight method. *Phys. Fluids* 17, 062107.

Zhang, X. 1999 Dynamics of growth and breakup of viscous pendant drops into air. *J. Colloid Sci.* 212, 107.

Zhang, X. & Basaran, O. A. 1995 An experimental study of dynamics of drop formation. *Phys. Fluids* 7, 1184.

Zhang, X., Padgett, R. S. & Basaran, O. A. 1996 Nonlinear deformation and breakup of stretching liquid bridges. *J. Fluid Mech.* 329, 207–245.

Zhao, H., Liu, H. F., Xu, J. L., Li, W. F. & Lin, K. F. 2015 Inhomogeneity in breakup of suspensions. *Phys. Fluids* 27, 063303.